Nuclear Instruments and Methods in Physics Research B 270 (2012) 75–92

Contents lists available at SciVerse ScienceDirect

Nuclear Instruments and Methods in Physics Research B

journal homepage: www.elsevier.com/locate/nimb

Calculations of electron stopping powers for 41 elemental solids over the 50 eV to 30 keV range with the full Penn algorithm

H. Shinotsuka [a], S. Tanuma [a], C.J. Powell [b,*], D.R. Penn [b]

[a] National Institute for Materials Science, 1-2-1 Sengen, Tsukuba, Ibaraki 305-0047, Japan
[b] National Institute of Standards and Technology, Gaithersburg, MD 20899, USA

ARTICLE INFO

Article history:
Received 2 May 2011
Received in revised form 19 September 2011
Available online 1 October 2011

Keyword:
Electron stopping powers

ABSTRACT

We present mass collision electron stopping powers (SPs) for 41 elemental solids (Li, Be, graphite, diamond, glassy C, Na, Mg, Al, Si, K, Sc, Ti, V, Cr, Fe, Co, Ni, Cu, Ge, Y, Nb, Mo, Ru, Rh, Pd, Ag, In, Sn, Cs, Gd, Tb, Dy, Hf, Ta, W, Re, Os, Ir, Pt, Au, and Bi) that were calculated from experimental energy-loss-function data with the full Penn algorithm for electron energies between 50 eV and 30 keV. Improved sets of energy-loss functions were used for 19 solids. Comparisons were made of these SPs with SPs calculated with the single-pole approximation, previous SP calculations, and experimental SPs. Generally satisfactory agreement was found with SPs from the single-pole approximation for energies above 100 eV, with other calculated SPs, and with measured SPs.

Published by Elsevier B.V.

1. Introduction

In previous papers [1,2], we reported calculations of collision electron stopping powers (SPs) over the 100 eV to 30 keV energy range in 41 elemental solids from their "optical" energy-loss functions (ELFs). These ELFs were obtained from experimental optical data representing the dependence of the inelastic-scattering probability on energy loss and the theoretical Lindhard dielectric function [3] to represent the dependence of the scattering probability on momentum transfer. SPs were calculated with Penn's algorithm that was originally developed for the calculation of electron inelastic mean free paths (IMFPs) [4]. Our SPs were determined using the single-pole approximation or so-called simple Penn algorithm (SPA) that was expected to be satisfactory for electron energies greater than about 100 eV [1,2]. We have extended this earlier work in two ways. First, we have calculated SPs with the full Penn algorithm (FPA) which should be valid for electron energies down to about 50 eV [5]. Second, we have adopted better sets of optical ELF data in recent IMFP calculations with the FPA for 19 of our 41 elemental solids [6], and we make use of the improved ELF data in the present work.

We report mass collision SPs calculated with the FPA for 41 elemental solids (Li, Be, graphite, diamond, glassy C, Na, Mg, Al, Si, K, Sc, Ti, V, Cr, Fe, Co, Ni, Cu, Ge, Y, Nb, Mo, Ru, Rh, Pd, Ag, In, Sn, Cs, Gd, Tb, Dy, Hf, Ta, W, Re, Os, Ir, Pt, Au, and Bi) over the 50 eV to 30 keV energy range with the same optical ELF data sets that were used in the IMFP calculations [6]. We give a brief description of our SP algorithm in the next section. The new SPs are presented in the following section where we compare SPs from the new ELFs (and the FPA) to SPs from the old ELFs (and the SPA) and compare SPs from the FPA to SPs from the SPA. We then make comparisons of our new SPs with values from previous SP calculations and measurements.

We note that the collision electron SP is an important parameter in radiation dosimetry [7] and in the modeling of electron transport in matter for many other applications. The SP has been used in Monte Carlo simulations of electron transport relevant to electron-probe microanalysis [8–10], Auger-electron spectroscopy [11,12], and dimensional metrology in the scanning electron microscope [13]. The Bethe SP equation [14–16] has been used extensively as a predictive tool for energies where it is expected to be valid (i.e., at energies much larger than the largest K-shell binding energy in the material of interest), but there is a scarcity of SP data at lower energies, typically less than 10 keV. SPs calculated from the Bethe equation are available from a National Institute of Standards and Technology (NIST) database [17] and ICRU Report 37 for electron energies of 10 keV and above [7]. It is thus important to have SPs available for lower energies in order to describe electron-solid interactions for a variety of applications.

2. Calculation of electron stopping powers with the full Penn algorithm

Penn developed an algorithm for the calculation of electron IMFPs from a model dielectric function $\varepsilon(q,\omega)$, a function of momentum transfer q and energy loss $\hbar\omega$ [4]. The energy dependence of the energy-loss function (ELF), $\mathrm{Im}[-1/\varepsilon(q,\omega)]$, can

* Corresponding author.
E-mail address: cedric.powell@nist.gov (C.J. Powell).

0168-583X/$ - see front matter Published by Elsevier B.V.
doi:10.1016/j.nimb.2011.09.016

be obtained from experimental optical data for the material of interest and the dependence of the ELF on q can be obtained from the Lindhard model dielectric function [3]. IMFPs were determined from a triple integration (the FPA) for energies down to about 50 eV, while a simpler procedure involving a single integration (the SPA) was judged satisfactory for electron energies larger than about 200 eV [4–6]. We utilized the SPA in our previous SP calculations, but now use the FPA to extend the energy range down to 50 eV.

We give here a summary of our implementation of the full Penn algorithm for SP calculations. We will use Hartree atomic units ($m_e = e = \hbar = 1$) where m_e is the electron rest mass, e is the elementary charge, and $\hbar$ is the reduced Planck constant.

The relativistic differential cross section (DCS) for inelastic scattering can be expressed as the sum of a longitudinal DCS and a transverse DCS [42]. For electron energies less than about 0.5 MeV, the transverse DCS can be neglected [18]. The relativistic inelastic DCS can then be written as [42]:

$$\frac{d^2\sigma}{d\omega dQ} \approx \frac{d^2\sigma_L}{d\omega dQ} = \frac{1}{v^2}\frac{1+Q/c^2}{Q(1+Q/2c^2)}\frac{1}{\pi N}\mathrm{Im}\left(\frac{-1}{\varepsilon(Q,\omega)}\right), \tag{1}$$

where Q is the recoil energy given by $Q(Q+2c^2) = (cq)^2$ [19,42], v is the electron velocity, c is the speed of light, and N is the number of atoms or molecules per unit volume. The last factor in Eq. (1) is the ELF expressed here as a function of energy loss ω and recoil energy Q. The relativistic DCS in Eq. (1) can be conveniently written as a function of momentum transfer q:

$$\frac{d^2\sigma}{d\omega dq} \approx \frac{2}{\pi N v^2}\mathrm{Im}\left(\frac{-1}{\varepsilon(q,\omega)}\right)\frac{1}{q}. \tag{2}$$

Stopping powers can be calculated with the FPA from the probability $p(T,\omega)$ for energy loss ω per unit distance traveled by an electron with relativistic kinetic energy T. This probability can be calculated from Eq. (2):

$$\begin{aligned} p(T,\omega) &= \frac{2}{\pi v^2}\int_{q_-}^{q_+}\frac{dq}{q}\mathrm{Im}\left[\frac{-1}{\varepsilon(q,\omega)}\right] \\ &= \frac{(1+T/c^2)^2}{1+T/(2c^2)}\frac{1}{\pi T}\int_{q_-}^{q_+}\frac{dq}{q}\mathrm{Im}\left[\frac{-1}{\varepsilon(q,\omega)}\right], \end{aligned} \tag{3}$$

where $q_\pm = \sqrt{T(2+T/c^2)} \pm \sqrt{(T-\omega)(2+(T-\omega)/c^2)}$. The collision stopping power, S, can be calculated from the following equation [20]:

$$S = \int_0^{\omega_{\max}} \omega p(T,\omega)d\omega, \tag{4}$$

where $\omega_{\max} = T - E_f$ and E_f is the Fermi energy.

The ELF in the FPA can be expressed as:

$$\mathrm{Im}\left[\frac{-1}{\varepsilon(q,\omega)}\right] = \int_0^\infty d\omega_p g(\omega_p)\mathrm{Im}\left[\frac{-1}{\varepsilon^L(q,\omega;\omega_p)}\right], \tag{5a}$$

where ε^L denotes the Lindhard model dielectric function of the free electron gas with plasmon energy $\omega_p(=\sqrt{4\pi n})$, n is the electron density, $g(\omega_p)$ is a coefficient introduced to satisfy the condition $\mathrm{Im}[-1/\varepsilon(q=0,\omega)] = \mathrm{Im}[-1/\varepsilon(\omega)]$, and $\mathrm{Im}[-1/\varepsilon(\omega)]$ is the optical energy-loss function. The coefficient $g(\omega_p)$ is then given by

$$g(\omega) = \frac{2}{\pi\omega}\mathrm{Im}\left[\frac{-1}{\varepsilon(\omega)}\right]. \tag{5b}$$

The Lindhard ELF, $\varepsilon^L = \varepsilon_1^L + i\varepsilon_2^L$, can be written as [3,21]:

$$\mathrm{Im}\left[\frac{-1}{\varepsilon^L(q,\omega;\omega_p)}\right] = \frac{\varepsilon_2^L}{(\varepsilon_1^L)^2+(\varepsilon_2^L)^2}, \tag{6a}$$

$$\varepsilon_1^L(q,\omega;\omega_p) = 1 + \frac{1}{\pi k_F z^2}\left[\frac{1}{2} + \frac{1}{8z}\left\{F\left(z-\frac{x}{4z}\right) + F\left(z+\frac{x}{4z}\right)\right\}\right], \tag{6b}$$

$$\varepsilon_2^L(q,\omega;\omega_p) = \frac{1}{8k_F z^3}\times\begin{cases} x & \text{for} \quad 0<x<4z(1-z) \\ 1-(z-(x/4z))^2 & \text{for} \quad |4z(1-z)|<x<4z(1+z), \\ 0 & \text{otherwise} \end{cases} \tag{6c}$$

where $F(t) = (1-t^2)\ln|(t+1)/(t-1)|$, $x = \omega/E_f$, $z = q/2k_F$, and k_F is the Fermi wave vector corresponding to a given ω_p .

We used the following expressions for the real and imaginary parts of the Lindhard dielectric function in our numerical calculations to reduce numerical errors at the limiting conditions of $\omega/qk_F(=u) \ll 1$ and $u \gg z+1$. When $u \ll 1$, ε_1^L and ε_2^L can be written as:

$$\varepsilon_1^L(q,\omega;\omega_p) = 1 + \frac{1}{\pi k_F z^2}\left[\frac{1}{2} + \frac{1}{4z}\left\{(1-z^2-u^2)\ln\left|\frac{z+1}{z-1}\right| + (z^2-u^2-1)\frac{2u^2 z}{(z^2-1)^2}\right\}\right] \tag{7a}$$

and

$$\varepsilon_2^L(q,\omega;\omega_p) = \frac{u}{2k_F z^2}. \tag{7b}$$

When $u \gg z+1$, ε_1^L and ε_2^L can be expressed as:

$$\varepsilon_1^L(q,\omega;\omega_p) = 1 - \frac{\omega_p^2}{\omega^2}\left\{1 + \left(z^2+\frac{3}{5}\right)\frac{1}{u^2}\right\} \tag{8a}$$

]and

$$\varepsilon_2^L(q,\omega;\omega_p) = 0. \tag{8b}$$

The energy-loss function in Eq. (5) from the FPA can be described as the sum of two contributions, one associated with the plasmon pole and the other with single-electron excitations [3,21,22]. That is,

$$\mathrm{Im}\left[\frac{-1}{\varepsilon(q,\omega)}\right] = \mathrm{Im}\left[\frac{-1}{\varepsilon(q,\omega)}\right]_{pl} + \mathrm{Im}\left[\frac{-1}{\varepsilon(q,\omega)}\right]_{se}. \tag{9}$$

The plasmon-pole contribution can be expressed as:

$$\mathrm{Im}\left[\frac{-1}{\varepsilon(q,\omega)}\right]_{pl} = g(\omega_0)\frac{\pi}{|\partial\varepsilon_1^L(q,\omega;\omega_p)/\partial\omega_p|_{\omega_p=\omega_0}}\Theta(q^-(\omega;\omega_0)-q), \tag{10a}$$

where

$$\frac{\partial\varepsilon_1^L(q,\omega;\omega_p)}{\partial\omega_p} = \frac{1}{3\pi\omega_p q z^2}\left\{\ln\left|\frac{Y_-+1}{Y_--1}\right| + \ln\left|\frac{Y_++1}{Y_+-1}\right|\right\}, \tag{10b}$$

and $Y_\pm \equiv z \pm x/4z$. To reduce calculation errors for $z/x \ll 1$ and for $z/x \gg 1$, we use the following equations:

$$\begin{aligned} &\ln\left|\frac{Y_-+1}{Y_--1}\right| + \ln\left|\frac{Y_++1}{Y_+-1}\right| \\ &\quad\approx -\frac{64}{3}za^2\{3+48(1+z^2)a^2+256(3+z^2)(1+3z^2)a^4\}, \end{aligned} \tag{10c}$$

where $a \equiv z/x$ when $z/x \ll 1$, and

$$\begin{aligned} &\ln\left|\frac{Y_-+1}{Y_--1}\right| + \ln\left|\frac{Y_++1}{Y_+-1}\right| \\ &\quad\approx \ln\left(\frac{z+1}{z-1}\right)^2 + 4zb^2\{1+(1+z^2)b^2+\frac{1}{3}(3+z^2)(1+3z^2)b^4\}, \end{aligned} \tag{10d}$$

where $b \equiv x/(z(z^2-1)$ when $z/x \gg 1$.

The single-electron-excitation contribution in Eq. (9) is given by:

$$\mathrm{Im}\left[\frac{-1}{\varepsilon(q,\omega)}\right]_{se} = \int_0^\infty d\omega_p g(\omega_p)\mathrm{Im}\left[\frac{-1}{\varepsilon^L(q,\omega;\omega_p)}\right]\Theta(q^+(\omega;\omega_p) - q)\Theta(q - q^-(\omega;\omega_p)), \tag{11a}$$

where

$$q^\pm(\omega;\omega_p) = \pm k_F(\omega_p) + \sqrt{k_F^2(\omega_p) + 2\omega}. \tag{11b}$$

Finally, when $Y_- = \pm 1$ (corresponding to quadratic curves in the (q,ω) plane separating single-electron excitations), we note that $F(\pm 1)$ is theoretically zero.

Several factors limit the reliability of SPs calculated from our model [2]. First, the Lindhard dielectric function model used in the FPA is expected to provide a useful approximation for the q-dependence of valence-electron excitations in free-electron-like materials but may be less reliable for non-free-electron-like solids. Second, use of the Lindhard model for describing the q-dependence of core-electron excitations is unlikely to be correct. Third, no account has been taken of exchange effects in inelastic scattering. Nevertheless, IMFPs calculated from optical ELFs with the FPA and the SPA are in good agreement with IMFPs determined experimentally by elastic-peak electron spectroscopy (EPES) in many elemental solids (including non-free-electron-like solids) for electron energies between 100 eV and 5 keV [23–25]. It is difficult to extend these comparisons to energies less than 100 eV due to limitations of the EPES technique [26].

3. Results

3.1. Stopping powers from the full Penn algorithm

We calculated values of the mass collision SP, S/ρ, where ρ is the mass density of the solid. Values of S/ρ were determined for 41 elemental solids (Li, Be, graphite, diamond, glassy C, Na, Mg, Al, Si, K, Sc, Ti, V, Cr, Fe, Co, Ni, Cu, Ge, Y, Nb, Mo, Ru, Rh, Pd, Ag, In, Sn, Cs, Gd, Tb, Dy, Hf, Ta, W, Re, Os, Ir, Pt, Au, and Bi) from the FPA. We utilized the same sets of optical ELFs as those used in our recent calculations of IMFPs for the same solids over the same energy range [6]. For 19 of our 41 solids (Ti, V, Cr, Fe, Ni, Y, Nb, Mo, Ru, Rh, Pd, Hf, Ta, W, Re, Os, Ir, Pt, and Au), we adopted improved sets of optical ELF data [6] compared to those used for our previous SP results [1,2]. We note that the new ELF data sets for Mg and Cu utilized in our recent IMFP calculations [6] had also been employed in our previous SP calculations for these solids [2]. Although we previously reported SPs for Zr [2], further analysis of its optical ELF data showed what we considered to be excessive errors in values of the f-sum and KK-sum [6] that we used to evaluate the internal consistency of a given ELF data set. Our SP values for Zr should therefore be considered only as rough estimates.

Values of S/ρ were calculated for relativistic electron kinetic energies between 10 eV and 30 keV (with respect to the Fermi level) at equal intervals on a logarithmic energy scale corresponding to increases of 10%. Table 1 shows the S/ρ values for our 41 elemental solids at electron energies between 50 eV and 30 keV. These SPs are given in units of MeVcm^2/g. The mass collision SPs can be converted to collision SPs (e.g., in eV/Å or eV/nm units) by multiplying by the material densities given in Table 1 of Ref. [6].

Plots of calculated mass collision SPs from the FPA as a function of energy are shown as solid lines in Figs. 1–7. SPs are included in these plots for energies less than 50 eV to illustrate trends, but these data are not considered as reliable [2]. The solid circles in Figs. 1–7 are SPs calculated with the SPA [1,2]. The SPs calculated with the FPA and SPA show similar systematic trends with atomic number. Sometimes, a single maximum is observed in the SP-versus-energy curves, sometimes secondary structures or multiple maxima are observed, and there are varying widths of the main maximum that generally occurs at energies between 10 eV and 300 eV. These trends have been discussed previously and are due to the varying contributions of valence-electron and different inner-shell excitations to the SP [2,27]. We also see in Figs. 1–7 that SPs from the SPA are larger than those from the FPA at energies in the vicinity of the maximum in each SP-versus-energy curve. On the other hand, SPs from the SPA are smaller than the corresponding SPs from the FPA for very low energies (typically less than 30 eV). This result is mainly due to differences in the ELF models used in each algorithm and will be discussed in more detail later.

The dashed lines in Figs. 1–7 show mass collision SPs calculated from the relativistic Bethe equation [2,14–16]:

$$S/\rho = \frac{784.58Z}{m_e v^2 A}[\ln(T/I)^2 + \ln(1+\tau/2) + G(\tau)] \quad (\text{in MeVcm}^2\text{g}^{-1}), \tag{12a}$$

where

$$G(\tau) = (1-\beta^2)[1 + \tau^2/8 - (2\tau+1)\ln 2], \tag{12b}$$

Z is the atomic number of the target, β is the electron velocity divided by the velocity of light, c, $\tau = T/m_e c^2$ is the ratio of the electron relativistic kinetic energy to its rest energy, and I is the mean excitation energy (MEE). Eq. (12) omits a density-effect correction which has been assumed here to be zero since its contribution is very small (less than 0.3% for our energy range [7]). SPs were calculated from Eq. (12) using MEEs listed in Table 4.3 of Ref. [7] except for the three carbon allotropes. SPs for glassy C, graphite and diamond were calculated with MEEs from our previous analysis [2]. SPs from Eq. (12) are shown in Figs. 1–7 from the minimum energies for which S is positive to 30 keV. As expected, we see generally good agreement between SPs from the FPA and those from Eq. (12) for energies larger than 10 keV. The root-mean-square (RMS) relative deviations between these calculated SPs and those from the Bethe equation were 9.1% and 8.7% at energies of 9.897 and 29.733 keV, respectively. These RMS deviations are almost the same as the corresponding deviations of 9.8% and 8.5% found previously between our SPs from the SPA and those from the Bethe equation [2].

3.2. Comparisons of stopping powers from new and old energy-loss functions

The energy-loss function (ELF) is the critical material-dependent parameter in our SP calculations. These ELFs were obtained from experimental optical data or ELF measurements for each solid. Sources of ELF data were given and details of our ELF analyses were described in a previous paper [6]. We comment now on differences between ELFs for 19 solids (Ti, V, Cr, Fe, Ni, Y, Nb, Mo, Ru, Rh, Pd, Hf, Ta, W, Re, Os, Ir, Pt, and Au) used here and the ELFs used for our previous SP calculations [1,2].

We first point out that we utilized photoabsorption data for these 19 solids at photon energies over 50 eV from Henke et al. [28] that are more recent than the data used previously [1,2]. For eight of these solids (Cr, Fe, Mo, Hf, Ta, W, Re, and Pt), it was necessary to make interpolations between two photon-energy (or electron energy-loss) regions, and we were guided in this process by measured transmission and reflection electron energy-loss spectroscopy (EELS) data. The resulting ELFs agreed better overall with the energy-loss data and resulted in smaller sum-rule errors for most of the solids than in our earlier SP and IMFP work [1,2,5,29]. For Ti, we selected optical data from a recent analysis of reflection EELS data by Werner et al. [30] for energy losses up to 54 eV because the resulting ELF was in much better agreement

Table 1
Calculated mass collision SPs (i.e., collision SPs divided by density) for the 41 elemental solids as a function of electron relativistic kinetic energy T.

T (eV)	Collision stopping power/density ($MeVcm^2g^{-1}$)						
	Li	Be	C (glassy)	C (graphite)	C (diamond)	Na	Mg
54.6	439.6	361.6	217.0	259.7	141.7	187.2	240.0
60.3	422.3	366.0	227.8	286.5	166.1	180.9	235.2
66.7	404.6	366.8	236.6	307.7	192.0	175.0	229.5
73.7	387.1	364.3	243.3	323.4	216.4	169.8	223.4
81.5	369.8	359.1	247.9	334.3	236.7	165.6	217.0
90.0	353.3	351.8	250.5	340.8	251.6	163.0	210.5
99.5	337.3	342.7	251.3	343.4	261.8	161.6	204.1
109.9	322.4	332.3	250.5	342.8	267.8	160.9	198.0
121.5	308.3	320.8	248.2	339.4	270.3	160.7	192.2
134.3	295.4	308.6	244.4	333.8	270.0	160.7	187.4
148.4	284.8	296.0	239.4	326.3	267.4	160.9	183.6
164.0	276.7	283.2	233.4	317.3	262.9	160.9	180.5
181.3	270.0	270.2	226.4	307.0	256.8	160.8	177.9
200.3	263.4	257.6	218.7	295.9	249.4	160.4	175.9
221.4	256.6	245.1	210.5	284.1	241.1	159.6	173.8
244.7	249.4	233.0	201.9	271.8	232.1	158.2	171.5
270.4	241.9	221.4	193.2	259.3	222.6	156.3	169.0
298.9	233.7	210.4	184.2	246.7	212.8	153.8	166.0
330.3	224.9	200.2	175.3	234.2	202.8	150.7	162.5
365.0	215.7	191.2	166.4	221.7	192.7	147.1	158.6
403.4	206.2	182.9	157.7	209.6	182.8	142.9	154.1
445.9	196.5	174.8	149.2	197.7	173.0	138.3	149.3
492.7	186.7	166.9	140.9	186.2	163.4	133.4	144.0
544.6	177.0	159.0	133.0	175.2	154.1	128.1	138.6
601.8	167.3	151.2	125.3	164.6	145.2	122.7	132.9
665.1	157.8	143.5	118.1	154.5	136.6	117.2	127.1
735.1	148.6	135.9	111.2	145.0	128.4	111.5	121.3
812.4	139.6	128.4	104.7	135.9	120.7	105.9	115.5
897.8	130.9	121.1	98.6	127.4	113.4	100.3	109.7
992.3	122.6	114.0	92.9	119.5	106.6	94.8	103.9
1096.6	114.6	107.2	87.8	112.2	100.3	89.4	98.3
1212.0	107.1	100.6	83.2	105.4	94.5	84.1	92.8
1339.4	99.9	94.2	78.8	99.0	88.9	79.1	87.4
1480.3	93.0	88.2	74.5	92.9	83.6	74.2	82.2
1636.0	86.6	82.4	70.3	87.1	78.6	69.5	77.2
1808.0	80.5	76.9	66.3	81.5	73.7	65.0	72.4
1998.2	74.8	71.7	62.4	76.3	69.1	60.7	67.8
2208.3	69.4	66.7	58.6	71.3	64.7	56.7	63.4
2440.6	64.4	62.1	55.0	66.5	60.5	52.9	59.3
2697.3	59.7	57.7	51.6	62.0	56.5	49.3	55.3
2981.0	55.3	53.6	48.3	57.8	52.7	45.9	51.5
3294.5	51.2	49.7	45.1	53.8	49.1	42.7	48.0
3640.9	47.4	46.1	42.1	50.0	45.7	39.7	44.7
4023.9	43.8	42.7	39.3	46.5	42.5	36.9	41.5
4447.1	40.5	39.6	36.6	43.2	39.5	34.3	38.6
4914.8	37.5	36.7	34.0	40.0	36.7	31.9	35.9
5431.7	34.6	33.9	31.7	37.1	34.1	29.7	33.3
6002.9	32.0	31.4	29.4	34.4	31.6	27.6	31.0
6634.2	29.5	29.0	27.3	31.9	29.3	25.7	28.8
7332.0	27.3	26.8	25.3	29.5	27.2	23.9	26.7
8103.1	25.2	24.8	23.5	27.3	25.2	22.2	24.8
8955.3	23.2	22.9	21.8	25.3	23.3	20.6	23.1
9897.1	21.4	21.2	20.2	23.4	21.6	19.1	21.4
10938.0	19.8	19.6	18.7	21.6	20.0	17.7	19.9
12088.4	18.3	18.1	17.3	20.0	18.5	16.5	18.5
13359.7	16.9	16.7	16.0	18.5	17.1	15.3	17.1
14764.8	15.6	15.4	14.9	17.1	15.8	14.2	15.9
16317.6	14.4	14.2	13.7	15.8	14.6	13.1	14.7
18033.7	13.3	13.1	12.7	14.6	13.5	12.2	13.7
19930.4	12.2	12.1	11.8	13.5	12.5	11.3	12.7
22026.5	11.3	11.2	10.9	12.5	11.6	10.5	11.8
24343.0	10.4	10.4	10.1	11.6	10.7	9.7	10.9
26903.2	9.65	9.60	9.36	10.7	9.92	9.01	10.1
29732.6	8.92	8.88	8.67	9.91	9.18	8.36	9.39
T (eV)	Al	Si	K	Sc	Ti	V	Cr
54.6	220.1	227.7	156.8	152.7	119.4	79.9	73.6
60.3	216.9	226.1	163.6	161.8	125.4	84.5	79.8
66.7	212.6	222.9	170.4	170.6	130.4	88.6	85.1
73.7	207.3	218.4	175.9	179.1	134.6	92.2	89.5
81.5	201.2	212.8	180.7	187.3	138.4	95.2	92.9
90.0	194.8	206.6	186.3	195.5	142.5	98.0	95.5
99.5	188.0	199.7	189.8	204.0	147.4	100.9	97.4

Table 1 (*continued*)

T (eV)	Al	Si	K	Sc	Ti	V	Cr
109.9	181.1	192.6	190.1	212.6	153.5	104.1	98.8
121.5	174.0	185.1	187.7	219.3	159.5	107.7	100.2
134.3	167.1	177.6	183.1	221.5	163.3	111.5	101.7
148.4	160.4	170.1	177.2	220.2	163.5	114.8	103.0
164.0	154.1	162.7	170.5	216.2	161.4	117.3	104.0
181.3	148.1	155.6	163.3	210.6	157.9	118.7	104.4
200.3	142.7	148.8	156.1	203.9	153.7	119.0	104.1
221.4	138.1	142.3	148.8	196.4	148.9	118.4	103.1
244.7	134.0	136.3	141.6	188.5	143.8	116.9	101.5
270.4	130.5	130.7	134.6	180.3	138.4	114.9	99.5
298.9	127.2	125.9	127.7	172.0	132.8	112.2	97.0
330.3	124.1	122.1	121.0	163.7	127.2	109.1	94.3
365.0	121.0	118.7	114.6	155.5	121.4	105.6	91.3
403.4	117.9	115.6	108.3	147.4	115.7	101.7	88.2
445.9	114.6	112.6	102.3	139.5	110.0	97.6	84.9
492.7	111.2	109.7	96.6	131.8	104.4	93.5	81.5
544.6	107.7	106.6	91.1	124.3	98.9	89.2	78.1
601.8	104.0	103.5	86.0	117.1	93.6	85.0	74.6
665.1	100.2	100.1	81.1	110.2	88.4	80.8	71.1
735.1	96.3	96.5	76.4	103.7	83.4	76.6	67.7
812.4	92.3	92.8	72.1	97.4	78.6	72.6	64.2
897.8	88.3	89.0	68.1	91.4	74.0	68.6	60.9
992.3	84.2	85.1	64.4	85.8	69.6	64.8	57.6
1096.6	80.1	81.1	61.1	80.5	65.4	61.1	54.5
1212.0	76.0	77.1	58.1	75.5	61.5	57.6	51.4
1339.4	72.0	73.1	55.4	70.8	57.7	54.2	48.5
1480.3	68.0	69.1	52.7	66.5	54.2	51.0	45.7
1636.0	64.1	65.3	50.2	62.5	51.0	48.0	43.0
1808.0	60.4	61.5	47.7	58.9	47.9	45.1	40.5
1998.2	56.7	57.8	45.2	55.5	45.2	42.5	38.1
2208.3	53.2	54.3	42.8	52.2	42.6	40.0	35.9
2440.6	49.9	50.9	40.5	49.2	40.2	37.8	33.9
2697.3	46.6	47.6	38.2	46.2	37.9	35.7	32.0
2981.0	43.6	44.5	35.9	43.4	35.7	33.7	30.3
3294.5	40.7	41.6	33.8	40.7	33.6	31.7	28.6
3640.9	37.9	38.8	31.7	38.1	31.5	29.8	27.0
4023.9	35.3	36.2	29.7	35.6	29.6	28.1	25.4
4447.1	32.9	33.7	27.8	33.3	27.7	26.3	23.9
4914.8	30.6	31.3	26.0	31.1	25.9	24.7	22.5
5431.7	28.5	29.1	24.3	29.0	24.3	23.1	21.1
6002.9	26.4	27.1	22.7	27.0	22.7	21.6	19.8
6634.2	24.6	25.2	21.1	25.2	21.1	20.2	18.5
7332.0	22.8	23.4	19.7	23.4	19.7	18.9	17.3
8103.1	21.2	21.7	18.3	21.8	18.4	17.6	16.2
8955.3	19.7	20.1	17.1	20.2	17.1	16.4	15.1
9897.1	18.3	18.7	15.9	18.8	15.9	15.3	14.1
10938.0	17.1	17.4	14.7	17.4	14.8	14.2	13.2
12088.4	15.8	16.1	13.7	16.2	13.7	13.2	12.3
13359.7	14.7	15.0	12.7	15.0	12.8	12.3	11.4
14764.8	13.7	13.9	11.8	13.9	11.9	11.4	10.6
16317.6	12.7	12.9	11.0	12.9	11.0	10.6	9.87
18033.7	11.8	12.0	10.2	12.0	10.2	9.87	9.18
19930.4	10.9	11.1	9.4	11.1	9.48	9.17	8.53
22026.5	10.2	10.3	8.8	10.3	8.80	8.52	7.93
24343.0	9.44	9.60	8.15	9.57	8.17	7.91	7.37
26903.2	8.76	8.92	7.58	8.88	7.59	7.35	6.86
29732.6	8.14	8.28	7.05	8.25	7.05	6.83	6.38

T (eV)	Fe	Co	Ni	Cu	Ge	Y
54.6	66.9	56.8	53.3	49.6	96.0	83.4
60.3	70.5	62.1	57.7	53.3	95.8	88.7
66.7	73.5	67.2	62.1	57.0	95.3	94.2
73.7	75.9	71.7	66.4	60.3	94.5	99.9
81.5	77.7	75.6	70.4	63.2	93.4	106.1
90.0	79.2	79.0	74.0	65.7	92.0	112.1
99.5	80.4	81.9	77.2	68.0	90.5	117.0
109.9	81.3	84.4	80.0	70.0	88.8	120.0
121.5	82.0	86.6	82.4	71.7	87.1	121.0
134.3	82.5	88.6	84.5	73.1	85.5	120.2
148.4	83.5	90.7	86.3	74.3	83.8	118.0
164.0	84.8	93.7	87.7	75.2	82.2	114.9
181.3	85.8	96.2	89.0	75.9	80.7	111.0
200.3	86.2	97.7	90.3	76.4	79.3	106.7
221.4	86.2	98.3	91.3	76.7	77.9	102.2
244.7	85.8	98.3	91.9	76.9	76.5	97.5

(*continued on next page*)

Table 1 (*continued*)

T (eV)	Fe	Co	Ni	Cu	Ge	Y
270.4	84.9	97.6	92.0	76.9	75.1	92.8
298.9	83.8	96.4	91.6	76.5	73.8	88.2
330.3	82.3	94.8	90.6	75.8	72.4	83.7
365.0	80.5	92.9	89.2	74.9	71.1	79.4
403.4	78.6	90.6	87.4	73.8	69.7	75.2
445.9	76.4	88.0	85.4	72.5	68.2	71.3
492.7	74.0	85.2	83.0	70.9	66.7	67.6
544.6	71.5	82.2	80.4	69.2	65.1	64.2
601.8	68.9	79.0	77.7	67.3	63.5	61.0
665.1	66.2	75.8	74.8	65.2	61.7	58.1
735.1	63.4	72.5	71.8	63.0	59.9	55.5
812.4	60.6	69.2	68.7	60.6	57.9	53.0
897.8	57.8	65.8	65.6	58.2	55.9	50.8
992.3	55.0	62.5	62.5	55.7	53.8	48.6
1096.6	52.2	59.3	59.4	53.2	51.7	46.5
1212.0	49.5	56.1	56.3	50.6	49.5	44.6
1339.4	46.8	52.9	53.2	48.1	47.2	42.6
1480.3	44.2	49.9	50.3	45.6	45.0	40.8
1636.0	41.7	47.0	47.4	43.2	42.8	38.9
1808.0	39.3	44.2	44.7	40.8	40.6	37.1
1998.2	37.0	41.5	42.0	38.5	38.4	35.2
2208.3	34.8	39.0	39.5	36.2	36.3	33.5
2440.6	32.8	36.6	37.1	34.1	34.2	31.7
2697.3	30.8	34.3	34.8	32.1	32.2	30.0
2981.0	29.0	32.2	32.6	30.1	30.3	28.3
3294.5	27.3	30.2	30.6	28.3	28.5	26.7
3640.9	25.8	28.4	28.7	26.6	26.7	25.1
4023.9	24.3	26.7	26.9	24.9	25.0	23.6
4447.1	22.9	25.0	25.3	23.4	23.5	22.1
4914.8	21.6	23.5	23.8	22.0	22.0	20.7
5431.7	20.3	22.1	22.3	20.7	20.6	19.4
6002.9	19.0	20.7	20.9	19.5	19.3	18.2
6634.2	17.9	19.4	19.6	18.3	18.1	17.0
7332.0	16.7	18.2	18.4	17.1	16.9	15.8
8103.1	15.7	17.0	17.2	16.0	15.9	14.8
8955.3	14.6	15.9	16.1	15.0	14.9	13.8
9897.1	13.7	14.8	15.0	14.0	13.9	12.9
10938.0	12.8	13.8	14.0	13.1	13.0	12.0
12088.4	11.9	12.9	13.1	12.3	12.1	11.2
13359.7	11.1	12.0	12.2	11.4	11.3	10.5
14764.8	10.3	11.2	11.4	10.7	10.6	9.77
16317.6	9.62	10.4	10.6	9.94	9.87	9.12
18033.7	8.96	9.65	9.84	9.25	9.20	8.51
19930.4	8.33	8.98	9.16	8.62	8.58	7.94
22026.5	7.75	8.35	8.52	8.02	7.99	7.40
24343.0	7.21	7.76	7.92	7.47	7.44	6.90
26903.2	6.71	7.22	7.37	6.95	6.93	6.44
29732.6	6.24	6.72	6.86	6.47	6.45	6.00

T (eV)	Nb	Mo	Ru	Rh	Pd	Ag	In
54.6	48.0	48.6	39.8	40.9	40.7	36.4	53.9
60.3	51.9	54.1	44.7	45.6	45.3	40.8	55.1
66.7	55.5	59.0	50.1	50.6	50.3	45.6	56.3
73.7	59.0	63.2	55.5	55.8	55.3	50.7	57.6
81.5	62.5	66.9	60.6	61.0	60.4	56.0	59.1
90.0	66.3	70.4	64.9	65.8	65.2	61.3	60.7
99.5	70.6	73.9	68.8	69.9	69.6	66.6	62.5
109.9	75.3	77.6	72.1	73.3	73.5	71.7	64.4
121.5	80.0	81.3	75.0	76.3	77.0	76.6	66.3
134.3	84.1	84.8	77.7	79.1	80.2	81.3	68.3
148.4	86.7	87.2	80.1	81.7	82.9	85.5	70.2
164.0	87.8	88.4	82.1	84.0	85.3	89.2	72.0
181.3	87.6	88.3	83.5	85.9	87.1	92.4	73.5
200.3	86.2	87.1	83.9	87.0	88.3	94.9	74.7
221.4	84.1	85.1	83.2	87.2	88.4	96.7	75.6
244.7	81.4	82.5	81.7	86.4	87.5	97.5	76.1
270.4	78.4	79.5	79.4	84.6	85.5	97.1	76.1
298.9	75.2	76.3	76.7	82.1	82.9	95.6	75.4
330.3	71.9	72.9	73.7	79.2	79.8	93.2	74.0
365.0	68.6	69.6	70.5	76.0	76.4	90.2	72.0
403.4	65.3	66.2	67.3	72.6	73.0	86.7	69.5
445.9	62.0	62.9	64.1	69.2	69.5	83.0	66.7
492.7	58.9	59.7	60.9	65.8	66.0	79.3	63.8
544.6	55.9	56.6	57.8	62.5	62.6	75.5	60.8
601.8	53.1	53.7	54.8	59.3	59.3	71.8	57.8

Table 1 (*continued*)

T (eV)	Nb	Mo	Ru	Rh	Pd	Ag	In
665.1	50.4	50.9	51.9	56.1	56.1	68.1	54.8
735.1	48.0	48.3	49.1	53.1	53.1	64.6	51.9
812.4	45.7	45.9	46.5	50.3	50.2	61.2	49.1
897.8	43.6	43.7	44.1	47.6	47.4	58.0	46.5
992.3	41.7	41.7	41.8	45.1	44.8	54.9	43.9
1096.6	39.9	39.8	39.6	42.7	42.4	52.1	41.5
1212.0	38.2	38.1	37.7	40.4	40.0	49.3	39.2
1339.4	36.6	36.5	36.0	38.4	37.9	46.8	37.0
1480.3	35.0	35.0	34.3	36.6	36.0	44.5	34.9
1636.0	33.5	33.5	32.8	34.8	34.2	42.5	33.0
1808.0	32.0	32.0	31.3	33.2	32.5	40.5	31.2
1998.2	30.5	30.6	29.9	31.7	31.0	38.5	29.6
2208.3	29.1	29.2	28.5	30.2	29.5	36.6	28.1
2440.6	27.7	27.8	27.2	28.8	28.1	34.8	26.6
2697.3	26.3	26.5	25.9	27.4	26.7	33.0	25.3
2981.0	24.9	25.1	24.6	26.0	25.4	31.2	24.0
3294.5	23.6	23.8	23.3	24.6	24.1	29.4	22.8
3640.9	22.3	22.5	22.1	23.3	22.8	27.7	21.6
4023.9	21.0	21.3	20.9	22.0	21.5	26.1	20.5
4447.1	19.8	20.0	19.7	20.8	20.3	24.6	19.4
4914.8	18.6	18.8	18.6	19.6	19.2	23.1	18.3
5431.7	17.5	17.7	17.5	18.4	18.1	21.6	17.2
6002.9	16.4	16.6	16.4	17.3	17.0	20.3	16.2
6634.2	15.4	15.6	15.4	16.2	15.9	19.0	15.3
7332.0	14.4	14.6	14.4	15.2	14.9	17.7	14.3
8103.1	13.4	13.6	13.5	14.3	14.0	16.5	13.4
8955.3	12.6	12.8	12.6	13.3	13.1	15.4	12.6
9897.1	11.7	11.9	11.8	12.5	12.2	14.4	11.8
10938.0	11.0	11.1	11.0	11.6	11.4	13.4	11.0
12088.4	10.2	10.4	10.3	10.9	10.7	12.5	10.3
13359.7	9.56	9.70	9.62	10.1	9.96	11.6	9.62
14764.8	8.93	9.05	8.97	9.45	9.30	10.8	8.98
16317.6	8.35	8.45	8.37	8.82	8.67	10.1	8.38
18033.7	7.80	7.90	7.81	8.23	8.09	9.38	7.81
19930.4	7.29	7.38	7.30	7.68	7.55	8.73	7.29
22026.5	6.81	6.89	6.81	7.17	7.04	8.13	6.80
24343.0	6.36	6.43	6.36	6.69	6.57	7.57	6.34
26903.2	5.94	6.01	5.94	6.25	6.14	7.06	5.92
29732.6	5.54	5.61	5.55	5.83	5.73	6.58	5.53
T (eV)	Sn	Cs	Gd	Tb	Dy	Hf	Ta
54.6	48.8	86.0	57.6	60.9	53.5	29.8	31.1
60.3	50.2	86.8	60.9	64.8	57.3	31.7	33.5
66.7	51.6	86.7	64.3	68.8	61.0	33.7	35.6
73.7	52.8	85.9	67.3	72.8	64.7	35.8	37.6
81.5	53.9	84.5	69.6	77.1	68.4	37.9	39.5
90.0	55.0	82.7	71.2	81.4	72.1	40.2	41.3
99.5	56.2	80.4	72.1	85.2	75.5	42.5	43.2
109.9	57.6	77.9	72.4	88.1	78.3	44.7	45.1
121.5	59.1	75.3	72.3	89.8	80.2	46.8	46.9
134.3	60.9	72.6	71.8	90.3	81.3	48.6	48.7
148.4	62.8	70.1	70.8	89.9	81.4	49.9	50.2
164.0	64.8	67.7	69.6	88.8	80.9	50.8	51.2
181.3	66.8	65.4	68.2	87.2	79.8	51.1	51.8
200.3	68.5	63.4	66.5	85.2	78.4	51.0	51.8
221.4	70.0	61.8	64.7	83.0	76.6	50.6	51.5
244.7	71.1	60.5	62.9	80.5	74.7	49.9	50.9
270.4	71.6	59.8	61.0	77.9	72.6	49.1	50.0
298.9	71.5	59.6	59.0	75.2	70.4	48.1	49.0
330.3	70.7	59.4	57.1	72.4	68.1	47.0	47.9
365.0	69.3	59.0	55.1	69.7	65.8	45.8	46.6
403.4	67.4	58.0	53.2	66.9	63.4	44.6	45.3
445.9	65.0	56.4	51.4	64.2	61.1	43.3	44.0
492.7	62.4	54.4	50.0	61.8	58.9	42.1	42.7
544.6	59.6	52.1	48.5	59.5	56.9	40.8	41.3
601.8	56.8	49.7	46.9	57.2	54.8	39.5	40.0
665.1	54.0	47.2	45.2	54.8	52.7	38.2	38.6
735.1	51.3	44.8	43.4	52.4	50.5	36.9	37.3
812.4	48.6	42.4	41.6	50.0	48.3	35.6	35.9
897.8	46.0	40.1	39.8	47.6	46.2	34.3	34.6
992.3	43.5	37.9	37.9	45.3	44.0	33.0	33.3
1096.6	41.1	35.8	36.1	43.0	41.9	31.7	32.0
1212.0	38.8	33.8	34.3	40.8	39.8	30.4	30.7
1339.4	36.7	31.9	32.6	38.6	37.8	29.1	29.4
1480.3	34.6	30.0	30.9	36.6	35.8	27.8	28.1

(*continued on next page*)

Table 1 (*continued*)

T (eV)	Sn	Cs	Gd	Tb	Dy	Hf	Ta
1636.0	32.7	28.3	29.3	34.5	33.9	26.6	26.9
1808.0	30.9	26.7	27.7	32.6	32.1	25.4	25.7
1998.2	29.2	25.1	26.2	30.8	30.3	24.2	24.5
2208.3	27.6	23.7	24.7	29.0	28.6	23.0	23.3
2440.6	26.2	22.3	23.3	27.3	26.9	21.8	22.1
2697.3	24.9	21.0	22.0	25.6	25.4	20.7	21.0
2981.0	23.6	19.8	20.7	24.1	23.9	19.6	19.9
3294.5	22.4	18.8	19.5	22.6	22.4	18.6	18.8
3640.9	21.3	17.8	18.3	21.2	21.1	17.5	17.8
4023.9	20.1	16.8	17.2	19.9	19.8	16.5	16.8
4447.1	19.1	15.9	16.2	18.7	18.5	15.6	15.8
4914.8	18.0	15.1	15.2	17.5	17.4	14.7	14.9
5431.7	17.0	14.3	14.3	16.4	16.3	13.8	14.0
6002.9	16.0	13.5	13.5	15.4	15.3	13.0	13.2
6634.2	15.1	12.7	12.7	14.5	14.3	12.2	12.4
7332.0	14.1	12.0	12.0	13.6	13.5	11.5	11.6
8103.1	13.3	11.3	11.3	12.8	12.7	10.8	10.9
8955.3	12.4	10.6	10.6	12.0	11.9	10.1	10.3
9897.1	11.6	10.0	10.0	11.3	11.2	9.54	9.64
10938.0	10.9	9.35	9.43	10.55	10.46	8.98	9.06
12088.4	10.2	8.77	8.87	9.89	9.81	8.45	8.52
13359.7	9.52	8.21	8.33	9.27	9.19	7.94	8.01
14764.8	8.88	7.68	7.82	8.67	8.61	7.46	7.52
16317.6	8.29	7.18	7.33	8.11	8.05	7.01	7.06
18033.7	7.74	6.71	6.87	7.58	7.53	6.58	6.62
19930.4	7.22	6.27	6.43	7.09	7.04	6.17	6.21
22026.5	6.73	5.86	6.02	6.62	6.57	5.78	5.82
24343.0	6.28	5.47	5.63	6.18	6.14	5.41	5.45
26903.2	5.86	5.11	5.27	5.77	5.73	5.07	5.11
29732.6	5.47	4.77	4.92	5.39	5.35	4.75	4.78
T (eV)	W	Re	Os	Ir	Pt	Au	Bi
54.6	27.0	24.4	21.1	21.7	23.7	24.3	40.8
60.3	30.3	28.1	23.9	24.6	26.4	26.9	42.1
66.7	33.3	32.0	26.9	27.8	29.4	29.7	43.2
73.7	36.0	35.3	29.9	31.0	32.5	32.6	44.3
81.5	38.2	38.0	32.6	34.2	35.5	35.7	45.4
90.0	39.9	40.3	35.0	36.9	38.1	38.7	46.5
99.5	41.4	42.3	36.8	39.1	40.3	41.6	47.8
109.9	42.9	44.0	38.3	41.0	42.1	44.2	49.0
121.5	44.3	45.6	39.7	42.6	43.6	46.5	50.4
134.3	45.8	47.1	41.1	44.0	44.9	48.4	51.9
148.4	47.3	48.4	42.5	45.1	45.9	49.9	53.4
164.0	48.4	49.5	43.7	46.0	46.6	51.0	54.8
181.3	49.1	50.2	44.5	46.6	47.0	51.8	56.0
200.3	49.3	50.5	44.9	47.0	47.1	52.1	56.9
221.4	49.1	50.3	44.9	46.9	46.9	52.0	57.3
244.7	48.5	49.7	44.6	46.4	46.5	51.5	57.4
270.4	47.7	48.8	43.9	45.7	45.8	50.7	57.0
298.9	46.8	47.7	43.0	44.7	44.8	49.7	56.1
330.3	45.6	46.5	42.0	43.5	43.7	48.4	54.9
365.0	44.5	45.2	40.9	42.2	42.5	47.0	53.5
403.4	43.2	43.8	39.7	40.8	41.1	45.4	51.7
445.9	41.9	42.5	38.5	39.4	39.7	43.7	49.8
492.7	40.7	41.1	37.3	38.1	38.3	42.0	47.8
544.6	39.4	39.7	36.1	36.7	37.0	40.3	45.8
601.8	38.1	38.3	34.9	35.4	35.6	38.6	43.7
665.1	36.8	37.0	33.7	34.1	34.3	37.0	41.7
735.1	35.6	35.6	32.5	32.9	33.1	35.4	39.7
812.4	34.3	34.3	31.4	31.7	31.9	34.0	37.8
897.8	33.1	33.0	30.3	30.6	30.7	32.5	36.0
992.3	31.9	31.8	29.2	29.4	29.5	31.2	34.3
1096.6	30.7	30.5	28.1	28.4	28.4	29.8	32.7
1212.0	29.5	29.3	27.0	27.3	27.3	28.6	31.2
1339.4	28.3	28.1	26.0	26.2	26.2	27.3	29.8
1480.3	27.1	26.9	24.9	25.2	25.2	26.1	28.4
1636.0	25.9	25.8	23.9	24.2	24.2	25.0	27.1
1808.0	24.8	24.6	22.9	23.2	23.1	23.9	25.9
1998.2	23.7	23.5	21.9	22.2	22.2	22.8	24.7
2208.3	22.6	22.4	20.9	21.2	21.2	21.8	23.5
2440.6	21.5	21.4	19.9	20.3	20.2	20.7	22.4
2697.3	20.4	20.3	19.0	19.3	19.3	19.7	21.3
2981.0	19.4	19.3	18.0	18.4	18.3	18.7	20.3
3294.5	18.4	18.3	17.1	17.4	17.4	17.8	19.2
3640.9	17.4	17.3	16.2	16.6	16.5	16.8	18.3

Table 1 (*continued*)

T (eV)	W	Re	Os	Ir	Pt	Au	Bi
4023.9	16.4	16.3	15.4	15.7	15.7	16.0	17.3
4447.1	15.5	15.4	14.5	14.8	14.8	15.1	16.4
4914.8	14.6	14.5	13.7	14.0	14.0	14.2	15.5
5431.7	13.7	13.7	12.9	13.2	13.2	13.4	14.6
6002.9	12.9	12.9	12.2	12.4	12.5	12.7	13.8
6634.2	12.2	12.1	11.5	11.7	11.7	11.9	12.9
7332.0	11.4	11.4	10.8	11.0	11.0	11.2	12.2
8103.1	10.7	10.7	10.1	10.3	10.4	10.5	11.4
8955.3	10.1	10.0	9.52	9.72	9.74	9.88	10.7
9897.1	9.46	9.42	8.94	9.13	9.14	9.27	10.0
10938.0	8.89	8.84	8.40	8.57	8.58	8.69	9.41
12088.4	8.36	8.31	7.89	8.05	8.06	8.16	8.82
13359.7	7.86	7.81	7.42	7.57	7.57	7.65	8.25
14764.8	7.38	7.34	6.98	7.11	7.11	7.19	7.73
16317.6	6.93	6.89	6.56	6.68	6.68	6.75	7.24
18033.7	6.51	6.47	6.16	6.27	6.28	6.34	6.78
19930.4	6.10	6.07	5.78	5.89	5.89	5.95	6.36
22026.5	5.72	5.69	5.42	5.53	5.53	5.58	5.95
24343.0	5.36	5.33	5.09	5.18	5.19	5.24	5.58
26903.2	5.02	5.00	4.77	4.86	4.86	4.91	5.23
29732.6	4.70	4.68	4.47	4.55	4.56	4.61	4.90

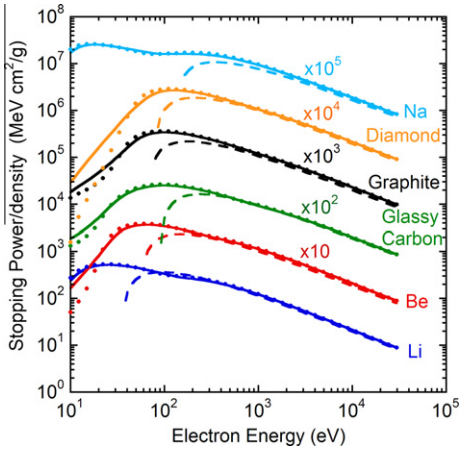

Fig. 1. Energy dependence of calculated mass collision stopping powers (or collision stopping powers divided by density) for Li, Be, glassy carbon, graphite, diamond, and Na. The solid lines show stopping powers calculated for each solid with the full Penn algorithm as a function of electron relativistic kinetic energy T. The solid circles show stopping powers calculated with the single-pole approximation. The dashed lines show stopping powers calculated from the relativistic Bethe equation (Eq. (12)).

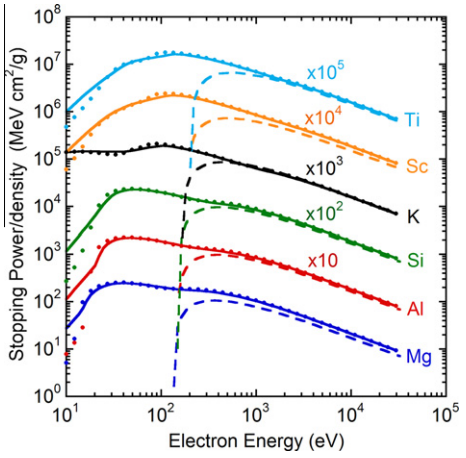

Fig. 2. Energy dependence of calculated mass collision stopping powers for Mg Al, Si, K, Sc, and Ti. See caption to Fig. 1.

with the reflection EELS data of Robins and Swan [31]. We also chose a set of optical data from Palik [32] for Au since this data set gave an ELF in better agreement with reflection EELS experiments [31] than the data set from Hagemann et al. [33] we used previously [1,2,5,29].

For two solids, Pd and V, there were large gaps in our previous ELFs (between 20 and 100 eV for Pd and between 40 and 100 eV for V). Our new ELF for Pd between 18 and 120 eV was obtained from an interpolation of ELF data [34] with a cubic spline function. The error in the f-sum for the new ELF was −2.3%, a value much smaller than that for the previous ELF (−12%) [29]. For V, we used a new set of optical data from Palik [32] for photon energies between 42.5 and 120 eV. We also chose new ELF data for photon energies less than 24 eV from Ref. [34] because this ELF better resembled transmission and reflection EELS data [30,35] than the previous ELF data. The resulting error in the f-sum was −0.8% (compared to the previous value of −20%) [29]. As a result, the new SPs for Pd and V are much larger than our previous SPs.

We checked the internal consistency of the new ELF data through use of the oscillator-strength sum rule (or f-sum rule) and a limiting form of the Kramers–Kronig integral (or KK-sum rule) [36–39]. The average root-mean-square (RMS) errors for the ELF data sets of our 41 solids were 4.2% and 7.7% based on the f-sum and KK-sum rules, respectively. These values are superior to the corresponding results for our previous ELFs (about 10% RMS error in both sum rules for 27 elemental solids) [5,29]. For over 80% of our 41 elemental solids, the ELFs satisfied the f-sum and KK-sum rules to better than 10%.

Fig. 8 shows ratios of SPs determined from the non-relativistic FPA, which are obtained from Eq. (3) when $T/c^2 \to 0$, and the new ELF data sets, S_{new}, to those calculated previously from the SPA and the old ELF data sets, S_{old}, [1,2] as a function of non-relativistic kinetic energy for the 19 elemental solids for which we adopted new ELF data. The largest changes occurred for Pd (where the SP increased by up to 58%), V (where the SP increased by up to 52%), and Re (where the SP decreased by up to 26%). These changes are the opposite of those found in similar comparisons of IMFPs (as shown in Fig. 11 of Ref. [6]). The changes in Fig. 8 result from two causes: use here of improved sets of ELF data [6] and differences in the SP calculation algorithms (the FPA and the SPA). The inset in

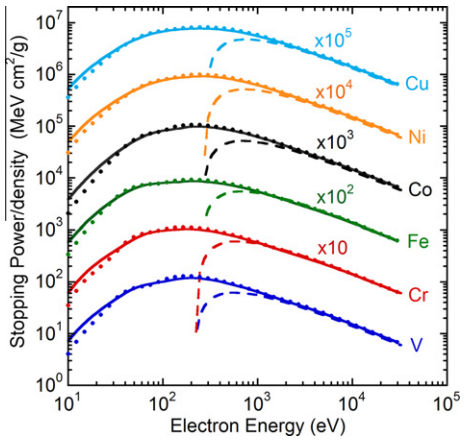

Fig. 3. Energy dependence of calculated mass collision stopping powers for V, Cr, Fe, Co, Ni, and Cu. See caption to Fig. 1.

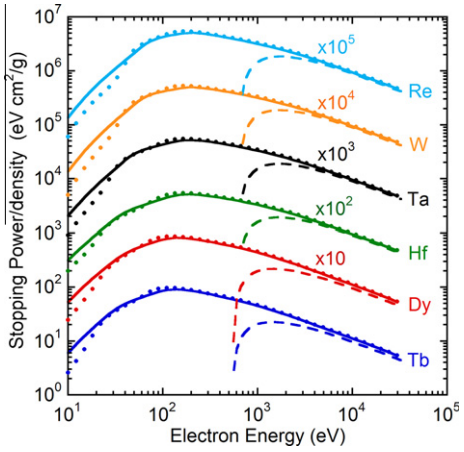

Fig. 6. Energy dependence of calculated mass collision stopping powers for Tb, Dy, Hf, Ta, W, and Re. See caption to Fig. 1.

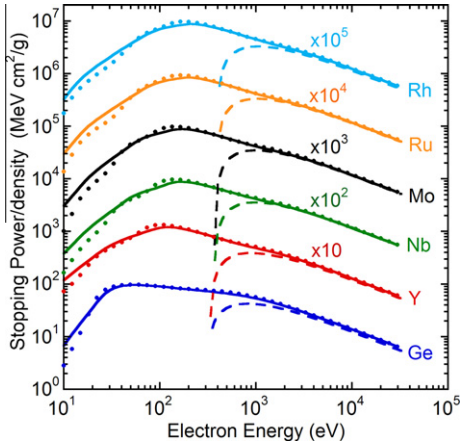

Fig. 4. Energy dependence of calculated mass collision stopping powers for Ge, Y, Nb, Mo, Ru, and Rh. See caption to Fig. 1.

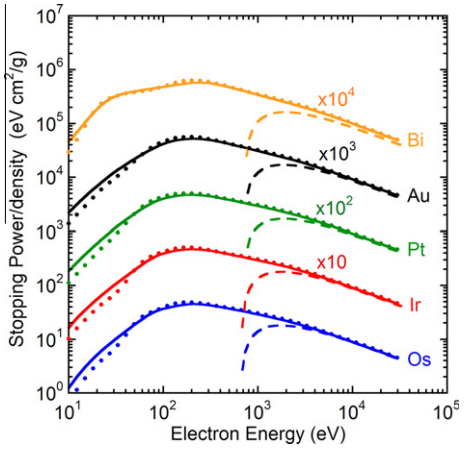

Fig. 7. Energy dependence of calculated mass collision stopping powers for Os, Ir, Pt, Au, and Bi. See caption to Fig. 1.

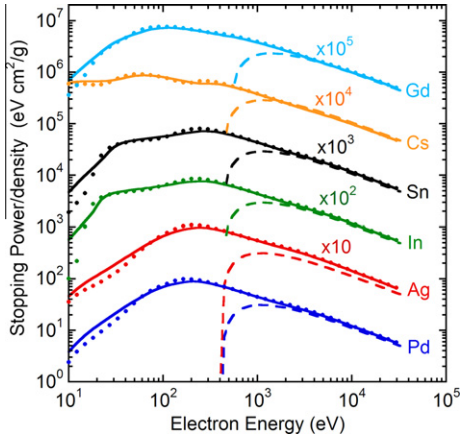

Fig. 5. Energy dependence of calculated mass collision stopping powers for Pd, Ag, In, Sn, Cs, and Gd. See caption to Fig. 1.

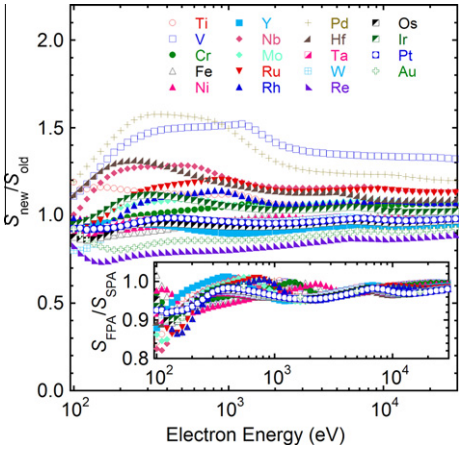

Fig. 8. Plots of ratios of SPs determined from the FPA and the new ELF data sets, S_{new}, to those calculated previously from the SPA and the old ELF data sets, S_{old}, [1,2] as a function of electron non-relativistic kinetic energy (i.e., $E = v^2/2$) for the 19 elemental solids for which we adopted new ELF data. The inset shows ratios of SPs from the FPA, S_{FPA}, to those from the SPA, S_{SPA}, for the same 19 solids. These SPs were calculated with the new ELFs for each algorithm.

Fig. 8 shows ratios of SPs from the FPA, S_{FPA}, to those from the SPA, S_{SPA}, for the 19 solids that were calculated using the new ELFs for each algorithm. We see that the SP changes are smaller than 10% and that most of the differences occur for energies less than 200 eV (as will be discussed further in the following section). Since the ratios S_{new}/S_{old} in Fig. 8 generally deviate from unity by more than the values of S_{FPA}/S_{SPA} in the inset, it is clear that most of the changes in S_{new}/S_{old} are due to the differences in the ELFs.

3.3. Comparison of stopping powers from the FPA and SPA

We now make comparisons of RMS differences between SPs calculated from the FPA and SPA using the same (new) ELF data set for each of our 41 solids. Relative percentage RMS differences, *RMS*, were calculated from

$$RMS = 100 \times \left[\sum_{i=1}^{41} \left(\frac{S_{SPA}(T)_i - S_{FPA}(T)_i}{S_{FPA}(T)_i} \right)^2 / 41 \right]^{0.5} \quad (\%) \qquad (13)$$

as a function of electron energy from 10 eV to 30 keV.

Fig. 9 shows plots of *RMS* as a function of relativistic kinetic energy. We see a steep decrease from about 50% for E = 10 eV to less than 10% for energies above 40 eV. The steep decrease must be due to the contributions of single-electron excitations to the SP that are neglected in the SPA (which only considers excitations at the plasmon pole). For energies above 40 eV, *RMS* generally decreases with increasing energy, reaching 1% at 30 keV. Three maxima are observed in Fig. 9 at energies of about 100 eV, 2 keV, and 10 keV. These maxima are due to the different energy positions of maxima and structure found in the SP plots from the FPA and SPA as a function of energy in Figs. 1–7.

3.4. Influence of electron exchange on stopping powers

It is important to know the effect of exchange between projectile and target electrons on SP calculations with the FPA. There is no consensus, however, on how to incorporate exchange effects within the dielectric formalism [6]. Nevertheless, we can estimate the influence of exchange on calculated SPs using the Born–Ochkur exchange correction [40,41].

The non-relativistic DCS with the Born–Ochkur correction can be written as [41]:

$$\frac{d^2\sigma}{dqd\omega} = \frac{C_{ex}}{\pi NE} \mathrm{Im}\left[\frac{-1}{\varepsilon(q,\omega)}\right]\frac{1}{q}, \qquad (14)$$

where E is the non-relativistic kinetic energy (i.e., $E = v^2/2$) and C_{ex} is the exchange correction factor given by

$$C_{ex} = 1 - \frac{q^2}{2E} + \left(\frac{q^2}{2E}\right)^2. \qquad (15)$$

We calculated SPs of Al, Cu, Ag, and Au with the exchange correction from Eqs. (14) and (15) and compared the results with corresponding SPs calculated without the exchange correction. Fig. 10 shows plots of ratios of SPs with the exchange correction to those without this correction as a function of non-relativistic kinetic energy. We see that SPs with the exchange correction are smaller than those without the exchange correction for these four solids and energies between 10 eV and 30 keV. Above 100 eV, SPs with the exchange correction are smaller than those without the exchange correction by less than about 10%. The SP ratios generally increase with increasing electron energy, reaching about 0.95 at 30 keV.

The influence of electron exchange on calculated SPs is almost the same as that found in IMFP calculations for electron energies between 50 and 100 eV [26]. We note, however, that the Born–Ochkur approximation is essentially a high-energy approximation. It is then not clear whether this approximation is useful for evaluating the exchange correction for energies less than 100 eV.

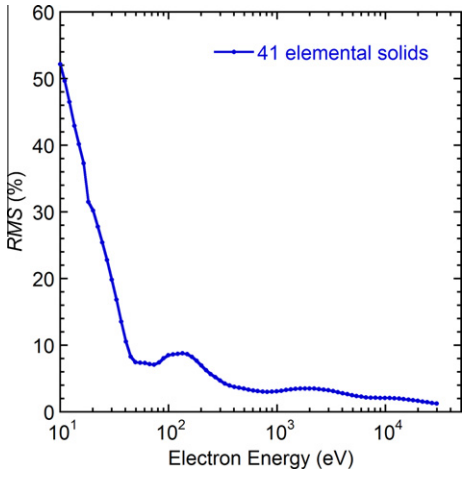

Fig. 9. The root-mean-square relative differences, *RMS*, of stopping powers calculated with the full Penn algorithm from stopping powers calculated with the single-pole approximation for the 41 elemental solids as a function of electron relativistic kinetic energy. The RMS differences were calculated from Eq. (13).

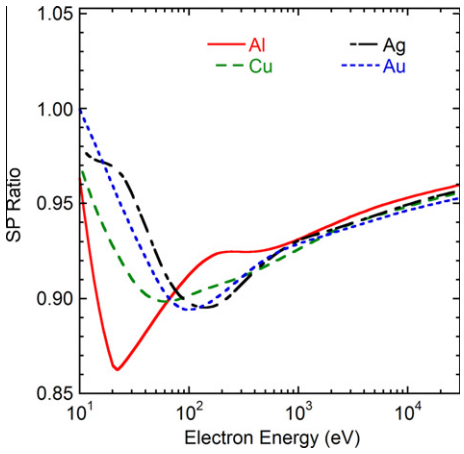

Fig. 10. Ratios of SPs calculated from the FPA with and without an exchange correction for Al, Cu, Ag, and Au as a function of non-relativistic electron kinetic energy (i.e., $E = v^2/2$).

4. Discussion

We will compare our calculated mass collision SPs with SPs from other calculations and from experiments. Although the FPA is expected only to provide a qualitative guide to SPs for energies less than about 50 eV, we show SPs calculated from the FPA for energies as low as 3 eV in Figs. 11–15 in order to make comparisons with available SP data.

4.1. Comparisons with calculated stopping powers

Mao et al. [21] calculated SPs of Al and Cu from 1 eV to 10 keV with the FPA. Fig. 11 shows comparisons of our SPs for Al and Cu calculated from the FPA and SPA with those of Mao et al. There is excellent agreement between our FPA SPs for Al and those of Mao et al. and satisfactory agreement for Cu. The slight differences for Cu at energies less than about 30 eV are probably due to the selection of different sets of optical ELF data in each calculation. As discussed in Section 3.3, the substantial differences in the SPs for Al from the FPA and SPA at energies less than 20 eV are associated with the contributions of single-electron excitations to the SP that occur at much lower energy losses than the relatively sharp plasmon peak at about 15 eV in the ELF. In contrast, there is broad structure in the Cu ELF, and a wide range of excitation energies contribute to the SP in the SPA calculation for Cu.

Fernandez-Varea et al. [42] calculated SPs for Al, Si, Cu, and Au for electron energies between 10 eV and 100 MeV. Their

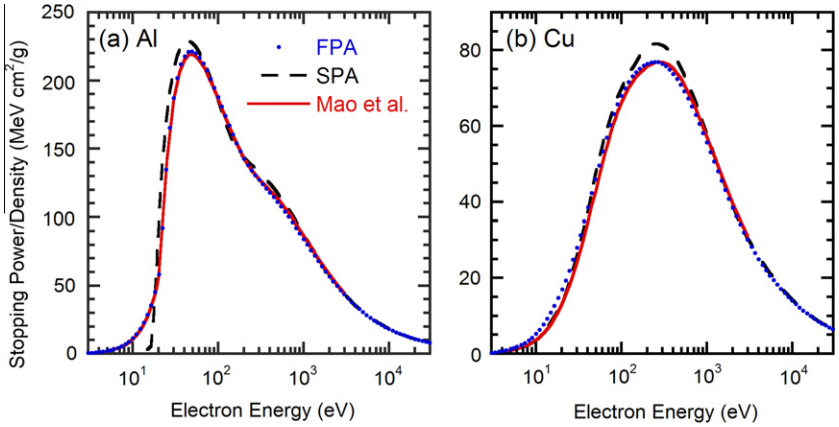

Fig. 11. Comparison of mass collision SPs calculated from optical data for (a) Al and (b) Cu with the full Penn algorithm by Mao et al. [21] (solid lines) as a function of electron relativistic kinetic energy with our SPs calculated with the single-pole approximation (long-dashed line) and the full Penn algorithm (solid circles).

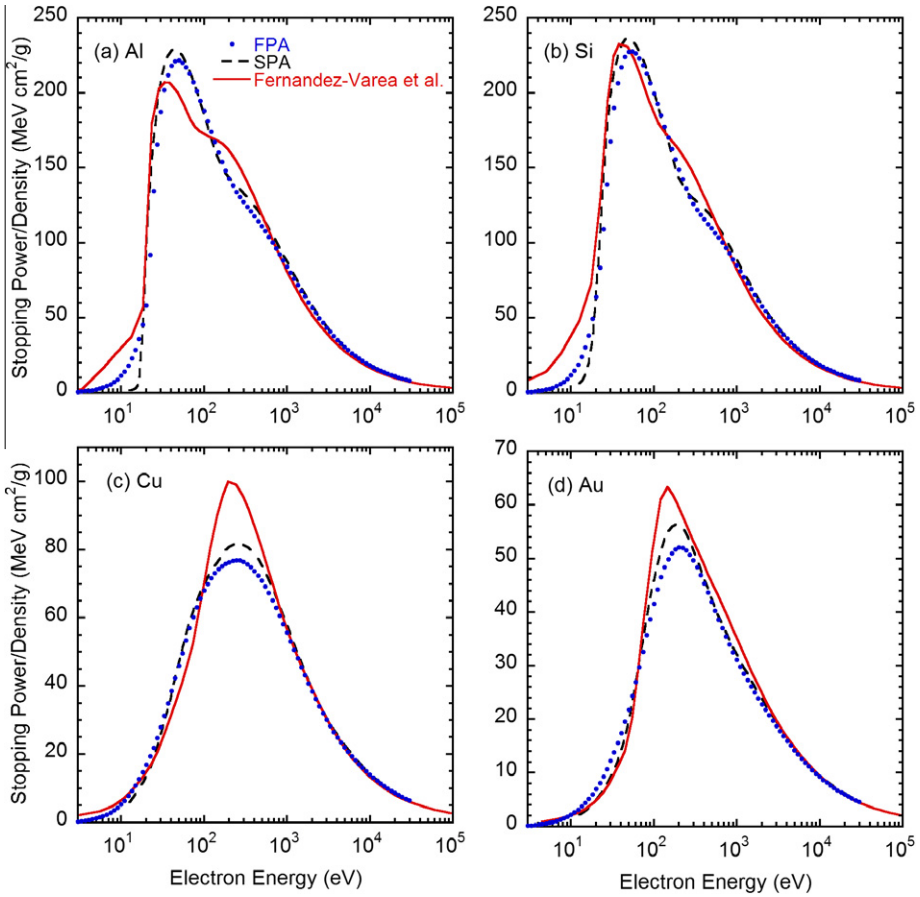

Fig. 12. Comparison of mass collision SPs calculated from optical data for (a) Al, (b) Si, (c) Cu, and (d) Au by Fernandez-Varea et al. [42] (solid lines) as a function of electron relativistic kinetic energy with our SPs that were obtained with the single-pole approximation (long-dashed line) and the full Penn algorithm (solid circles).

calculations were based on a so-called "N-oscillator" model in which different dispersion relations were applied for valence-electron excitations and inner-shell excitations. They also included a correction for electron exchange to cross sections for inner-shell excitations. We compare their SPs with our SPs from the FPA and SPA in Fig. 12. For energies over 1 keV, the SPs of Fernandez-Varea et al. for Al, Si, Cu, and Au are in excellent agreement with our values from the FPA. For Al and Si, there are differences in the shapes of the SP versus energy curves in the vicinity of 100 eV. These differences might be associated with the "switch energies" of 73 eV and 99 eV for Al and Si, respectively, used by Fernandez-Varea et al. to represent the demarcation between their models for valence-electron and inner-shell excitations. For Cu and Au, the switch energies are 74 eV and 54 eV, respectively, but there are no obvious changes of slope in the SP-versus-energy curves for these solids in Fig. 12. This difference from the Al and Si behavior occurs because the switch energies for Cu and Au occur in a structureless region of their ELFs. Tan et al. [43] reported SP

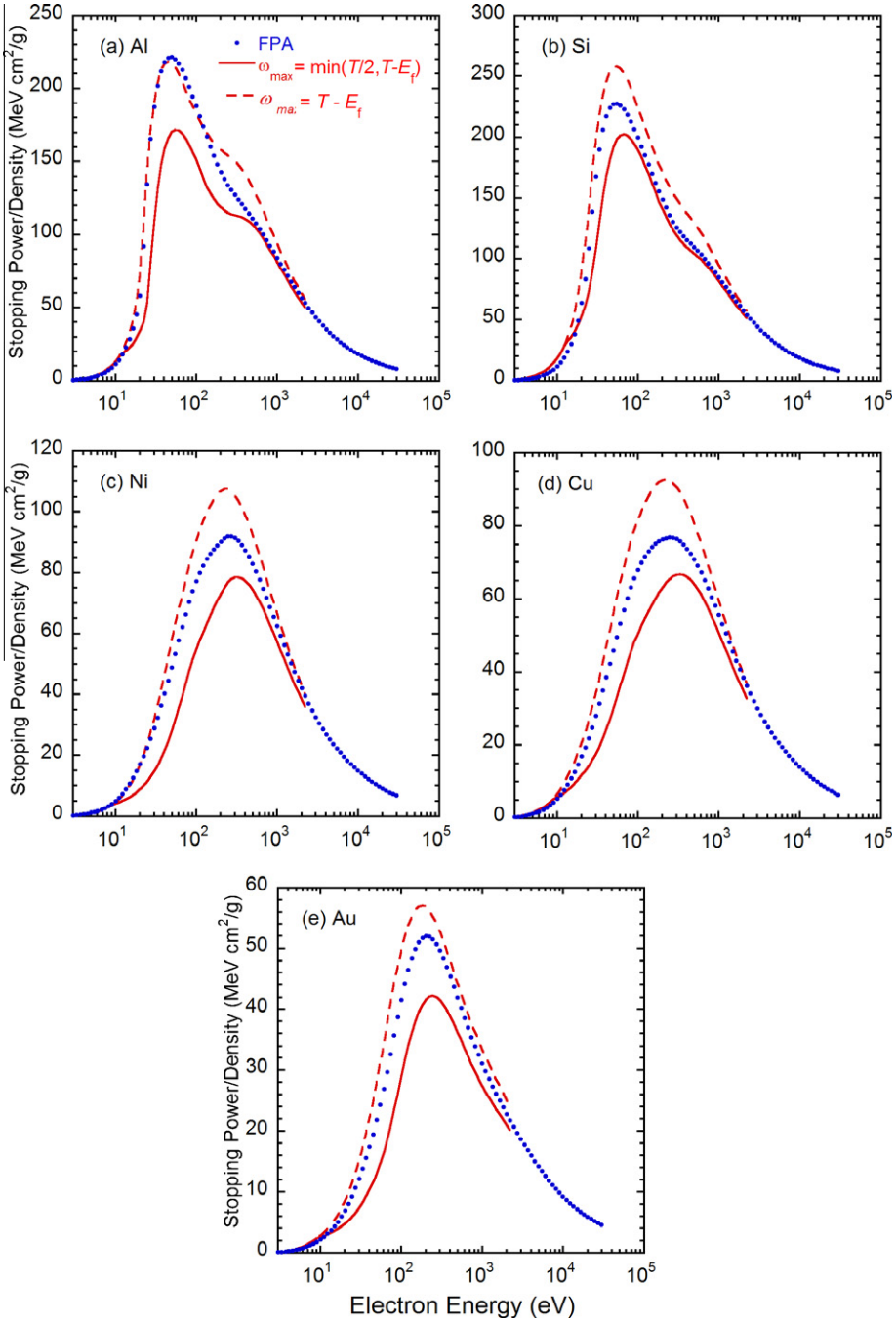

Fig. 13. Comparison of our mass collision SPs obtained from the full Penn algorithm (solid circles) as a function of relativistic kinetic energy for (a) Al, (b) Si, (c) Ni, (d) Cu, and (e) Au with SPs calculated from the Mermin-ELF model with $\omega_{\max} = \min(T/2, T - E_f)$ (solid lines) and with $\omega_{\max} = T - E_f$ (long-dashed lines).

calculations for a group of organic compounds with the SPA and two types of exchange correction [41,44]. They found that inclusion of exchange reduced their computed SPs by an average of 28%, 9%, and 9% for energies of 100 eV, 1 keV, and 10 keV, respectively. These differences are in good agreement with our estimates of electron exchange effect for SPs as shown in Fig. 10 except at 100 eV. Their calculations were done up to $\omega_{max} = T/2$ in Eq. (4). They must then obtain larger SPs at a low energy such as 100 eV if they used the same $\omega_{max}(= T - E_f)$ value as we used. We will refer later to this issue in comparison of SPs from the FPA and from the Mermin model. Nevertheless, the maximum SPs of Fernandez-Varea et al. (with an exchange correction) for Cu and Au are larger than our corresponding maximum SPs from the FPA (without an exchange correction). For Si and Al, however, there is close agreement in the maximum SPs from Fernandez-Varea et al. and our calculations with the FPA. It therefore appears that the exchange correction must be smaller than differences due to other factors (e.g., differences in optical ELFs and differences in the models). We have also pointed out in our related IMFP calculations that correlation and exchange should be treated in an integrated manner together with information on the band structure of the solid [6].

Abril et al. [45] proposed an algorithm for IMFP and SP calculations based largely on a Mermin-model dielectric function for the ELF (Mermin-ELF model) [46]. The Mermin function is an improvement over the Lindhard dielectric function used here in that it accounts for the finite lifetimes of the various excitations. Their

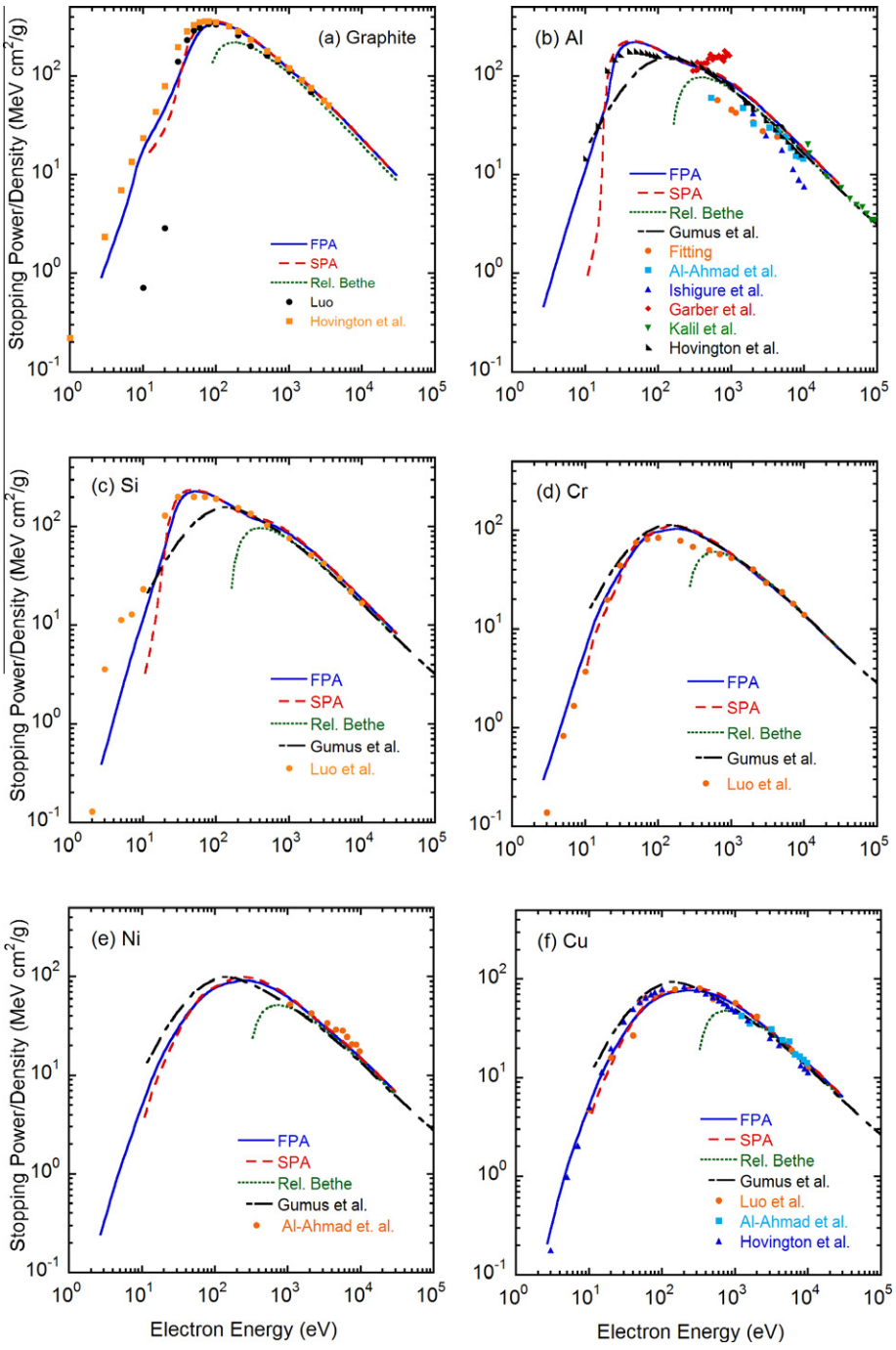

Fig. 14. Mass collision stopping powers for (a) graphite, (b) Al, (c) Si, (d) Cr, (e) Ni, and (f) Cu as a function of electron relativistic kinetic energy. The dotted lines show SPs from the relativistic Bethe formula (Eq. (12)), and the solid and long-dashed lines show our SPs from the full Penn algorithm and the single-pole approximation, respectively. The long-short dashed lines show SPs calculated from a modified Bethe-Bloch SP equation and expressions for the effective atomic electron number and the effective mean excitation energies [51]. The symbols indicated SPs derived from the experiments of Luo et al. [53] (for Si, Cr, and Cu), Luo [54] (for graphite), Hovington et al. [55] (for graphite, Al, and Cu), Kalil et al. [57] (for Al), Al-Ahmad and Watt [58] (for Al, Ni, and Cu), Garber et al. [59] (for Al), Fitting [60] (for Al), and Ishigure et al. [61] (for Al).

model of Mermin energy-loss functions was combined with generalized oscillator strengths (MELF-GOSs) to fit experimental ELF data. The part of an experimental ELF ascribed to excitations of outer-shell electrons was fitted with a linear combination of Mermin-type ELFs, and the part associated with excitations of inner-shell electrons was fitted with hydrogenic generalized oscillator strengths [47].

We have calculated SPs for Al, Si, Ni, Cu, and Au with the Mermin-ELF model using the parameters for outer-electron excitations given in Table 1 of Ref. [48] for Al, Si, Ni, and Cu and Table 1 of Ref. [49] for Au; these parameters were determined from fits to optical ELFs for excitation energies up to about 1 keV and thus include the contributions of several inner shells. In our calculations we ignored the contributions of GOSs for inner-shell ionization of the K shells of Al and Si, of the K and L shells of Ni and Cu, and of the K, L, and M shells of Au. We estimated their contribution to be less than a few percent for electron energies less than 2 keV for Ni and Cu and less than 10 keV for Al, Si, and Au.

Fig. 13 shows comparisons between SPs from the FPA (solid symbols) and from the Mermin-ELF model (solid and dashed lines)

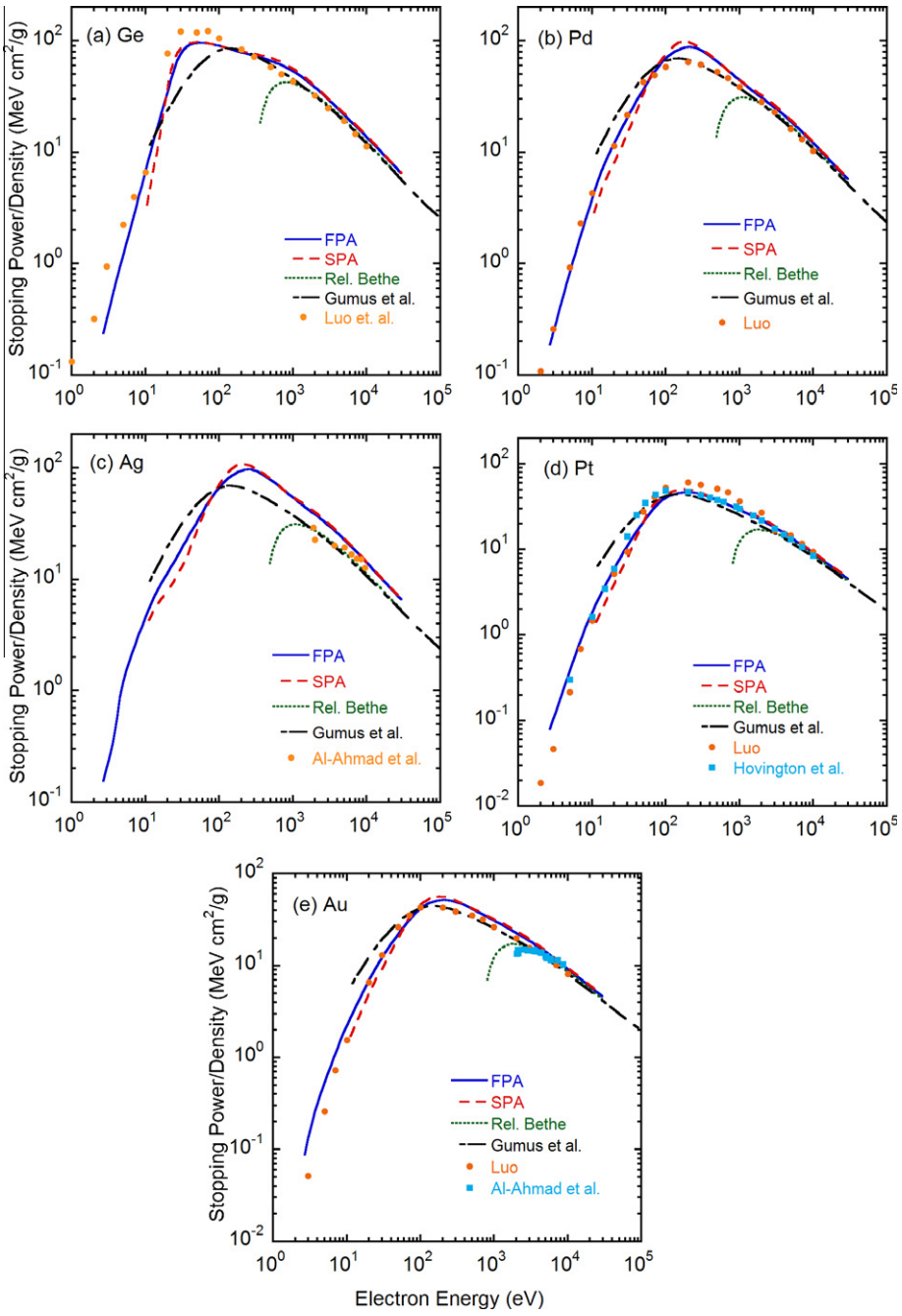

Fig. 15. Mass collision stopping powers for (a) Ge, (b) Pd, (c) Ag, (d) Pt, and (e) Au as a function of electron relativistic kinetic energy. The dotted lines shows SPs from the relativistic Bethe formula (Eq. (12)), and the solid and long-dashed lines show our SPs from the full Penn algorithm and the single-pole approximation, respectively. The long-short dashed lines show SPs calculated from a modified Bethe–Bloch SP equation and expressions for the effective atomic electron number and the effective mean excitation energies [51]. The symbols indicated SPs derived from the experiments of Luo et al. [53] (for Ge), Luo [54] (for Pd, Pt, and Au), Hovington et al. [55] (for Pt), and Al-Ahmad and Watt [58] for Ag and Au).

for Al, Si, Ni, Cu, and Au using two choices for the upper limit $\omega_{\max}$ for excitation energy in the latter SP calculations. One value of $\omega_{\max}$ was $\omega_{\max} = \min(T/2, T - E_f)$, as recommended by Denton et al. [50], while the other was $\omega_{\max} = T - E_f$ as chosen here for evaluation of Eq. (2). Denton et al. chose the former limit to avoid consideration of secondary electrons having energies larger than inelastically-scattered primary electrons. Larger energy transfers are possible, however, although secondary electrons may then be indistinguishable from scattered primary electrons, either in experiments or in model calculations of electron energy spectra. We believe that the upper limit $\omega_{\max} = T - E_f$ is more appropriate for the SP calculation, as we have chosen here for the results in Figs. 1–7.

Fig. 13 indicates that SPs from the FPA are smaller than those from the Mermin-ELF model with the same upper limit $\omega_{\max} = T - E_f$ for Si, Ni, Cu, and Au. These differences are generally less than 20% for energies over 50 eV and may be associated with different q-dependences of the ELF in the two models. For Al, SPs from the Mermin-ELF model (with $\omega_{\max} = T - E_f$) and from the FPA are in good agreement for energies less than 200 eV. This agreement, in contrast to the results for Si, Ni, Cu, and Au, may be fortuitous because of the relatively poorer fit for Al of the

Mermin-ELF to the optical ELF (particularly around the volume-plasmon energy-loss peak between 12 and 17 eV) than for the other four solids.

Fig. 13 also shows that calculated SPs from the FPA are larger by up to about 250% than those from the Mermin-ELF model with $\omega_{\max} = \min(T/2, T - E_f)$ for energies between 20 eV and 1 keV. For energies above 1 keV, there is generally good agreement between SPs from the two approaches. In contrast, we previously found much better agreement between IMFPs calculated with the FPA for Al and Au [6] and those reported by Denton et al. [50] who used the Mermin-ELF model with the same parameters as those given in Refs. [48] and [49]. This observation suggests that choice of the upper limit ω_{max} is more significant in SP calculations than in IMFP calculations because of the greater relative contributions of possible large-energy-loss excitations to the SP [the factor ω in Eq. (4)] than to the IMFP. Fig. 13 indicates that the choice of the upper limit is most important for electron energies between about 20 eV and about 1 keV.

Gumus et al. [51] calculated SPs for Al, Si, Cr, Ni, Cu, Ge, Pd, Ag, Pt, and Au for electron energies between 10 eV and 100 MeV. Their calculations were performed using a modified Bethe–Bloch SP expression and analytical expressions for the effective atomic number and the effective mean excitation energy of each material. We show their SPs in Figs. 14 and 15 together with our SPs (and the experimental SPs discussed in the next section). For energies over 200 eV, the SPs of Gumus et al. for Al, Si, Cr, Cu, Ge, and Pt, are in good agreement with our values from the FPA and SPA. We also see that the SPs of Gumus et al. for the other solids are smaller than our SPs from the FPA for energies above 200 eV. For energies between 10 and 200 eV, the SPs of Gumus et al. for Al, Si, and Ge are smaller than our SPs while they obtain larger SPs for the other solids. Except for Ag, there is generally good agreement between the Gumus et al. SPs and our SPs from the FPA and SPA for energies over 200 eV. Since their calculations were made with a modified Bethe formula that is usually applied for much higher energies, 200 eV must be an effective low-energy limit for their approach.

For Ag, there are larger differences between our SPs from the FPA and those of Gumus et al. at energies above 200 eV, as stated above. Since the SPs of Ag for Gumus et al. are in good agreement with SPs from the relativistic Bethe formula (Eq. (12)) for energies above 5 keV, the differences with our SPs might be due to uncertainties in the experimental ELF data for Ag (despite relatively small errors in the f-sum and KK-sum rules [6]).

4.2. Comparison with experimental stopping powers

We compare calculated SPs from the FPA for graphite, Al, Si, Cr, Ni, Cu, Ge, Pd, Ag, Pt, and Au in Figs. 14 and 15 with experimental SP data that were mostly obtained from Joy's database [52]. We previously made similar comparisons of SPs from the SPA for Al, Si, Cr, Ni, Cu, Ge, Pd, Ag, Pt, and Au and for electron energies between 100 eV and 30 keV [1]. We will therefore emphasize comparisons here between SPs from the FPA and measured SPs as well as comparisons for energies less than 100 eV. Comparisons will also be made with SPs from the relativistic Bethe equation (Eq. (12)) using MEEs listed in Table 4.3 of Ref. [7] except graphite. The MEE value for graphite was obtained from our previous work [2]. We also show SPs from the SPA in Figs. 14 and 15 so that similarities and differences with the FPA results are visible.

The experimental SPs in Figs. 14 and 15 can be classified into two groups. Almost all of the experimental SPs for energies less than 1 keV were reported by Luo et al. [53], Luo [54], and Hovington et al. [55,56]. These SPs are based on measurements of transmission electron energy-loss spectra of 100 or 200 keV electrons transmitted through thin specimen films. The energy-loss spectra for energy losses up to 1 keV and for the angular acceptance of their spectrometer were analyzed to obtain the single-scattering ELF. These ELFs were extended to larger energy losses using atomic X-ray absorption data. Checks were made to ensure that the ELFs satisfied the expected sum rules. SPs were then calculated from the experimental ELFs without consideration of any q-dependence other than that expected from the scattering kinematics. Their SP calculation, although derived from experimental ELFs, is very similar in principle to our SP calculation from optical ELFs. The other group of measured SPs in Figs. 14 and 15 was obtained from calorimetric methods for Al, Ni, Cu, Ag, and Au [57,58], from a novel thin-film method in which currents to electrodes at the top and bottom surfaces of a film were measured (and with the electrodes separated from the film by thin insulating layers) for Al [59], from analyses of energy distributions of electrons transmitted through a thin Al film with a retarding-field analyzer [60], and from analyses of energy distributions of electrons transmitted through a thin Al film at various scattering angles [61].

We see generally excellent agreement between our SPs from the FPA and the Joy SPs for energies larger than about 10 eV and in some cases (Cu, Pd, and Pt) for lower energies. However, the excellent agreement at energies near 10 eV is very likely fortuitous because our SP calculations with the FPA ignored the effects of electron exchange and correlation that must be important at such low energies. Some small but systematic differences are found at energies between 10 and 100 eV for graphite, Al, Si, and Ge, and similar differences can be seen for larger energies for Cr, Pd, Pt, and Au. Generally good agreement is found between our SPs from the FPA and the SPs measured by calorimetry for Al, Ni, Cu, Ag, and Au for energies between about 4 and 30 keV, but there are disagreements between our SPs and those of Al-Ahmad and Watt [58] for Al, Ag, and Au at lower energies.

The comparisons in Fig. 14 for Al show a wide spread in measured SPs for the same material as measured by different methods. The measured SPs at a given energy can differ by a factor of more than two, and the energy dependence of the SPs reported by Garber et al. [59] differs from those obtained by other methods (including the FPA). Given this disparity in SP results for a single material, we believe that there is satisfactory agreement between SPs from the FPA and the measured SPs. Definitive experimental tests are still required, however, to determine whether and how any exchange correction should be included in the SP calculation, as discussed in Sections 3.4 and 4.1. Further experimental tests are also required to distinguish differences in SPs corresponding to different choices of the upper limit ω_{max} in Eq. (4), as discussed in Section 4.1.

We note that there is good agreement between SPs from the FPA and SPA in Figs. 14 and 15 for all solids except Al, Si, and Ge at energies less than 20 eV. These solids have strong and narrow plasmon peaks in their energy-loss spectra. As discussed in Sections 3.3 and 4.1, substantial differences can occur for such solids between SPs determined from the FPA and SPA because SPs from the SPA do not have contributions from single-electron excitations.

Finally, we see satisfactory agreement in Figs. 14 and 15 between SPs from the relativistic Bethe equation (Eq. (12)), SPs calculated from the FPA, and most measured SPs for energies larger than about 5 keV for low-Z and most medium-Z elements (graphite, Al, Si, Cr, Ni, Cu, Ge, and Pd) and for energies larger than about 10 keV for high-Z elements (Pt and Au). For Ag, however, there are larger differences between SPs from the FPA and those from Eq. (12) at energies above 5 keV than for the other solids. These differences might be due to uncertainties in the experimental ELF data for Ag [6].

5. Summary

We have reported mass collision electron SPs for Li, Be, graphite, diamond, glassy C, Na, Mg, Al, Si, K, Sc, Ti, V, Cr, Fe, Co, Ni, Cu, Ge, Y,

Nb, Mo, Ru, Rh, Pd, Ag, In, Sn, Cs, Gd, Tb, Dy, Hf, Ta, W, Re, Os, Ir, Pt, Au, and Bi over the 50 eV to 30 keV energy range. These SPs were calculated from ELFs determined from experimental optical data or ELF measurements [6] with the full Penn algorithm [4]. For 19 of our 41 solids, we adopted improved sets of optical ELF data [6] over those used for our previous SP calculations with the single-pole approximation or simple Penn algorithm [1,2]. The largest changes occurred for Pd (where the SP increased by up to 58%), V (where the SP increased by up to 52%), and Re (where the SP decreased by up to 26%).

We made comparisons of RMS differences between SPs calculated from the FPA and SPA using the same ELF data sets for the calculations with each algorithm. For energies above 50 eV, the RMS relative differences were less than 10% and generally decreased with increasing energy, reaching 1% at 30 keV.

We compared our calculated SPs with results from other calculations. Mao et al. [21] calculated SPs of Al and Cu from 1 eV to 10 keV with the FPA. There was excellent agreement between our SPs from the FPA for Al and those of Mao et al. and satisfactory agreement for Cu. Fernandez-Varea et al. [42] calculated SPs of Al, Si, Cu, and Au for electron energies between 10 eV and 100 MeV with their N-oscillator model. For energies over 1 keV, the SPs of Fernandez-Varea et al. for Al, Si, Cu, and Au were in excellent agreement with our values from the FPA. For Al and Si, there were differences in the shapes of the SP-versus-energy curves in the vicinity of 100 eV. These differences might be associated with the "switch energies" of 73 and 99 eV for Al and Si, respectively, used by Fernandez-Varea et al. to represent the demarcation between their models for valence-electron and inner-shell excitations. Their maximum values of the SPs for Al and Si were in reasonable agreement with our maximum values, but their maximum values for Cu and Au were larger than our maximum values.

Abril et al. [45] developed an algorithm for IMFP and SP calculations based on a Mermin-model dielectric function (Mermin-ELF model) [46]. We calculated SPs for Al, Si, Ni, Cu, and Au with the Mermin-ELF model using the parameters for outer-electron excitations adopted by the Abril group [48,49]. These calculations were performed with two choices for the upper limit $\omega_{\max}$ for excitation energy, one being $\omega_{\max} = \min(T/2, T - E_f)$, as recommended by Denton et al. [50], while the other was $\omega_{\max} = T - E_f$ as chosen here for our SP calculations. The differences between SPs with the latter choice of $\omega_{\max}$ and our SPs from the FPA were generally less than 20% for Si, Ni, Cu, and Au at energies above 50 eV and for Al at energies above 200 eV. In similar comparisons of SPs with the former choice of ω_{max}, our SPs were larger than those from the Mermin-ELF model by up to 250% for energies between 20 eV and 1 keV. There was, however, good agreement for energies less than 20 eV for Al, Si, Cu, and Au or less than 10 eV for Ni and greater than 1 keV for the five solids. We believe that $\omega_{\max} = T - E_f$ is the more appropriate choice for the upper limit.

We compared our SPs calculated from the FPA for graphite, Al, Si, Cr, Ni, Cu, Ge, Pd, Ag, Pt, and Au with values derived from available experimental data. Most of these comparisons were made with SPs derived by Joy et al. [52–56] from ELFs obtained from analyses of energy-loss spectra measured by transmission of 100 or 200 keV electrons through thin specimen films. We found generally excellent agreement between SPs derived in this way and our SPs from the FPA for energies larger than about 10 eV, although there were small but systematic differences for some solids between 10 and 100 eV. There was satisfactory agreement between our calculated SPs and values determined from calorimetry experiments for Al, Ni, Cu, Ag, and Au [57,58] at energies between 4 keV and 30 keV, but there were disagreements with the experimental SPs for Al, Ag, and Au [58] at lower energies. SPs have been measured by other methods for only one material (Al) [59–61], but the reported SPs at a particular energy can differ by a factor of more than two.

Finally, we compared our calculated SPs with values from the relativistic Bethe equation with recommended mean excitation energies derived from a wide variety of experimental data [7] and from our previous analysis for the three carbon allotropes [2]. The RMS relative deviations between our calculated SPs and values from the Bethe equation were 9.1% and 8.7% for energies of 9.897 and 29.733 keV, respectively. Satisfactory agreement was found between SPs from the Bethe equation, our SPs, and most measured SPs for energies larger than about 5 keV for low-Z and most medium-Z elements (graphite, Al, Si, Cr, Ni, Cu, Ge, and Pd) and for energies larger than about 10 keV for high-Z elements (Pt and Au). Larger differences between SPs from the Bethe equation and from the FPA were found for Ag at energies above 5 keV, presumably due to uncertainties in the experimental ELF data set for Ag.

Acknowledgments

We thank Drs. Z.-J. Ding and J. M. Fernandez-Varea for supplying numerical data and Drs. I. Abril and C. D. Denton for useful comments and discussions.

References

[1] S. Tanuma, C.J. Powell, D.R. Penn, Surf. Interface Anal. 37 (2005) 978.
[2] S. Tanuma, C.J. Powell, D.R. Penn, J. Appl. Phys. 103 (2008) 063707.
[3] J. Lindhard, K. Dan, Vidensk. Selsk. Mat.-Fys. Medd. 28 (8) (1954) 1.
[4] D.R. Penn, Phys. Rev. B 35 (1987) 482.
[5] S. Tanuma, C.J. Powell, D.R. Penn, Surf. Interface Anal. 17 (1991) 911.
[6] S. Tanuma, C.J. Powell, D.R. Penn, Surf. Interface Anal. 43 (2011) 689.
[7] M.J. Berger, M. Inokuti, H.H. Anderson, H. Bichsel, J.A. Dennis, D. Power, S.M. Seltzer, J.E. Turner. Stopping Powers for Electrons and Positrons, ICRU Report 37, International Commission on Radiation Units and Measurements, Bethesda, 1984.
[8] R. Gauvin, Surf. Interface Anal. 37 (2005) 875.
[9] N.W.M. Ritchie, Surf. Interface Anal. 37 (2005) 1006.
[10] F. Salvat, X. Llovet, J.M. Fernandez-Varea, J. Sempau, Surf. Interface Anal. 37 (2005) 1054.
[11] A. Jablonski, C.J. Powell, S. Tanuma, Surf. Interface Anal. 37 (2005) 861.
[12] A. Jablonski, C.J. Powell, Surf. Sci. 604 (2010) 1928.
[13] J.S. Villarrubia, A.E. Vladar, M.T. Postek, Surf. Interface Anal. 37 (2005) 951.
[14] H. Bethe, Ann. Physik (Leipzig) 5 (1930) 325.
[15] H. Bethe, Handbuch der Physik, in: H. Geiger, K. Scheel (Eds.), vol. 24/1, Springer, Berlin, 1933, p. 273.
[16] H.A. Bethe J. Ashkin, Experimental Nuclear Physics, in: E. Segre (Ed.), Wiley, New York, 1953, p. 166.
[17] M.J. Berger, J.S. Coursey, M.A. Zucker, J. Chang, Stopping Power and Range Tables for Electrons, Positrons, and Helium Ions, version 1.2.3, <http://www.nist.gov/pml/data/star/index.cfm>, 2005.
[18] J.M. Fernandez-Varea, D. Liljequist, S. Csillag, R. Raty, F. Salvat, Nucl. Instrum. Methods Phys. Res. B 108 (1996) 35.
[19] U. Fano, Ann. Rev. Nucl. Sci. 13 (1963) 1.
[20] M. Dapor, Electron-Beam Interactions with Solids, Springer, Berlin, 2003.
[21] S.F. Mao, Y.G. Li, R.G. Zeng, Z.J. Ding, J. Appl. Phys. 104 (2008) 114907.
[22] K.O. Jensen, A.B. Walker, Surf. Sci. 292 (1993) 83.
[23] S. Tanuma, T. Shiratori, T. Kimura, K. Goto, S. Ichimura, C.J. Powell, Surf. Interface Anal. 37 (2005) 833.
[24] W.S.M. Werner, C. Tomastik, T. Cabela, G. Richter, H. Störi, Surf. Sci. 470 (2000) L123.
[25] W.S.M. Werner, C. Tomastik, T. Cabela, G. Richter, H. Störi, J. Electron Spectrosc. Relat. Phenom. 113 (2001) 127.
[26] C.J. Powell, A. Jablonski, J. Phys. Chem. Ref. Data 28 (1999) 19.
[27] K. Kumagai, S. Tanuma, C.J. Powell, Nucl. Instrum. Methods Phys. Res. B 267 (2009) 167.
[28] B.L. Henke, J.C. Davis, E.M. Gullikson, R.C.C. Perera, Lawrence Berkeley Laboratory Report 26259 (1988);
B.L. Henke, E.M. Gullikson, J.C. Davis, At. Data Nucl. Data Tables 54 (1993) 181.
[29] S. Tanuma, C.J. Powell, D.R. Penn, Surf. Interface Anal. 11 (1988) 577.
[30] W.S.M. Werner, K. Glantschnig, C. Ambrosch-Draxl, J. Phys. Chem. Ref. Data. 38 (2009) 1013.
[31] J.L. Robins, J.B. Swan, Proc. Phys. Soc. (London) 76 (1960) 857.
[32] E.D. Palik (Ed.), Handbook of Optical Constants of Solids, Academic Press, New York, 1985.
[33] H.-J. Hagemann, W. Gudat, and C. Kunz, Deutsches Elektronen-Synchrotron Report SR-74/7, Hamburg, 1974, (unpublished).;
H.–J. Hagemann, W. Gudat, C. Kunz, J. Opt. Soc. Am. 65 (1975) 742.

[34] E.D. Palik (Ed.), Handbook of Optical Constants of Solids II, Academic Press, New York, 1991.
[35] C.C. Ahn (Ed.), Transmission Electron Energy Loss Spectrometry in Materials Science and the EELS ATLAS, Wiley-VCH, Germany, 2004.
[36] D.Y. Smith, Handbook of Optical Constants of Solids in: E.D. Palik (Ed.), Academic Press, New York, 1985, p. 210.
[37] G.D. Mahan, Many-Particle Physics, Plenum, New York, 2000. p. 358.
[38] S. Tanuma, C.J. Powell, D.R. Penn, Surf. Interface Anal. 17 (1991) 929.
[39] S. Tanuma, C.J. Powell, D.R. Penn, J. Electron Spectrosc. Relat. Phenom. 62 (1993) 95.
[40] V.I. Ochkur, Sov. Phys. JETP 18 (1964) 503.
[41] J.M. Fernandez-Varea, R. Mayol, D. Liljequist, F. Salvat, J. Phys.: Condens. Matter. 5 (1993) 3593.
[42] J.M. Fernandez-Varea, F. Salvat, M. Dingfelder, D. Liljequist, Nucl. Instrum. Methods Phys. Res. B 229 (2005) 187.
[43] Z. Tan, Y. Xia, M. Zhao, X. Liu, F. Li, B. Huang, Y. Ji, Nucl. Instrum. Methods Phys. Res. B 222 (2005) 47.
[44] J.C. Ashley, V.E. Anderson, J. Electron Spectrosc. Relat.Phenom. 24 (1981) 127.
[45] I. Abril, R. Garcia-Molina, C.D. Denton, F.J. Pérez-Pérez, N.R. Arista, Phys. Rev. A 58 (1998) 357.
[46] N.D. Mermin, Phys. Rev. B 1 (1970) 2362.
[47] R.F. Egerton, Electron Energy Loss Spectroscopy in the Electron Microscope, Plenum Press, New York, 1989.
[48] C.D. Denton, I. Abril, J.C. Moreno-Marín, S. Heredia-Avalos, R. Garcia-Molina, Phys. Stat. Sol. (b) 245 (2008) 1498.
[49] S. Heredia-Avalos, I. Abril, C.D. Denton, J.C. Moreno-Marín, R. Garcia-Molina, J. Phys.: Condens. Matter. 19 (2007) 466205.
[50] C.D. Denton, I. Abril, R. Garcia-Molina, J.C. Moreno-Marin, S. Heredia-Avalos, Surf. Interface Anal. 40 (2008) 1481.
[51] H. Hasan Gumus, O. Kabadayi, Vacuum 85 (2010) 245.
[52] D.C. Joy, http://web.utk.edu/~srcutk/htm/interact.htm, April, 2008.
[53] S. Luo, X. Zhang, D.C. Joy, Rad. Eff. Defects Solids 117 (1991) 235.
[54] S. Luo, Study of Electron-Solid Interactions, PhD Thesis, University of Tennessee, May, 1994.
[55] P. Hovington, D. C. Joy, R. Gauvin, and N. Evans, unpublished data summarized in Ref. [56].
[56] D.C. Joy, S. Luo, R. Gauvin, P. Hovington, N. Evans, Scanning Microsc. 10 (1996) 653.
[57] F. Kalil, W.G. Stone, H.H. Hubell, R.D. Birkhoff, Oak Ridge National Laboratory Report 2731 (1959).
[58] K.O. Al-Ahmad, R.E. Watt, J. Phys. D: Appl. Phys. 16 (1983) 2257.
[59] F.W. Garber, M.Y. Nakai, J.A. Harter, R.D. Birkhoff, J. Appl. Phys. 42 (1971) 1149.
[60] H.-J. Fitting, Phys. Stat. Sol. (a) 26 (1974) 525.
[61] N. Ishigure, C. Mori, T. Watanabe, J. Phys. Soc. Japan. 44 (1978) 973.